NASA/TP-2000-210096

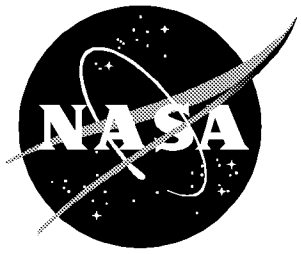

Characterization of Advanced Avalanche Photodiodes for Water Vapor Lidar Receivers

Tamer F. Refaat
Old Dominion University, Norfolk, Virginia

Gary E. Halama and Russell J. DeYoung
Langley Research Center, Hampton, Virginia

July 2000

The NASA STI Program Office . . . in Profile

Since its founding, NASA has been dedicated to the advancement of aeronautics and space science. The NASA Scientific and Technical Information (STI) Program Office plays a key part in helping NASA maintain this important role.

The NASA STI Program Office is operated by Langley Research Center, the lead center for NASA's scientific and technical information. The NASA STI Program Office provides access to the NASA STI Database, the largest collection of aeronautical and space science STI in the world. The Program Office is also NASA's institutional mechanism for disseminating the results of its research and development activities. These results are published by NASA in the NASA STI Report Series, which includes the following report types:

- TECHNICAL PUBLICATION. Reports of completed research or a major significant phase of research that present the results of NASA programs and include extensive data or theoretical analysis. Includes compilations of significant scientific and technical data and information deemed to be of continuing reference value. NASA counterpart of peer-reviewed formal professional papers, but having less stringent limitations on manuscript length and extent of graphic presentations.

- TECHNICAL MEMORANDUM. Scientific and technical findings that are preliminary or of specialized interest, e.g., quick release reports, working papers, and bibliographies that contain minimal annotation. Does not contain extensive analysis.

- CONTRACTOR REPORT. Scientific and technical findings by NASA-sponsored contractors and grantees.

- CONFERENCE PUBLICATION. Collected papers from scientific and technical conferences, symposia, seminars, or other meetings sponsored or co-sponsored by NASA.

- SPECIAL PUBLICATION. Scientific, technical, or historical information from NASA programs, projects, and missions, often concerned with subjects having substantial public interest.

- TECHNICAL TRANSLATION. English-language translations of foreign scientific and technical material pertinent to NASA's mission.

Specialized services that complement the STI Program Office's diverse offerings include creating custom thesauri, building customized databases, organizing and publishing research results . . . even providing videos.

For more information about the NASA STI Program Office, see the following:

- Access the NASA STI Program Home Page at ***http://www.sti.nasa.gov***

- Email your question via the Internet to help@sti.nasa.gov

- Fax your question to the NASA STI Help Desk at (301) 621-0134

- Telephone the NASA STI Help Desk at (301) 621-0390

- Write to:
  NASA STI Help Desk
  NASA Center for AeroSpace Information
  7121 Standard Drive
  Hanover, MD 21076-1320

NASA/TP-2000-210096

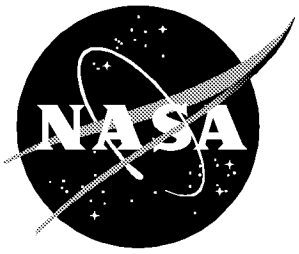

Characterization of Advanced Avalanche Photodiodes for Water Vapor Lidar Receivers

Tamer F. Refaat
Old Dominion University, Norfolk, Virginia

Gary E. Halama and Russell J. DeYoung
Langley Research Center, Hampton, Virginia

National Aeronautics and
Space Administration

Langley Research Center
Hampton, Virginia 23681-2199

July 2000

Available from:

NASA Center for AeroSpace Information (CASI)
7121 Standard Drive
Hanover, MD 21076-1320
(301) 621-0390

National Technical Information Service (NTIS)
5285 Port Royal Road
Springfield, VA 22161-2171
(703) 605-6000

Contents

Abstract

Development of advanced differential absorption lidar (DIAL) receivers is very important to increase the accuracy of atmospheric water vapor measurements. A major component of such receivers is the optical detector. In the near-infrared wavelength range avalanche photodiodes (APD's) are the best choice for higher signal-to-noise ratio, where there are many water vapor absorption lines. In this study, characterization experiments were performed to evaluate a group of silicon-based APD's. The APD's have different structures representative of different manufacturers. The experiments include set-ups to calibrate these devices, as well as characterization of the effects of voltage bias and temperature on the responsivity, surface scans, noise measurements, and frequency response measurements. For each experiment, the setup, procedure, data analysis, and results are given and discussed. This research was done to choose a suitable APD detector for the development of an advanced atmospheric water vapor differential absorption lidar detection system operating either at 720, 820, or 940 nm. The results point out the benefits of using the super low ionization ratio (SLIK) structure APD for its lower noise-equivalent power, which was found to be on the order of 2 to 4 $fW/Hz^{1/2}$, with an appropriate optical system and electronics. The water vapor detection systems signal-to-noise ratio will increase by a factor of 10.

1. Introduction

Water vapor is an important molecular species in the Earth's atmosphere, which is primarily located in the troposphere (part of the atmosphere extending from the surface of the Earth to an altitude of about 18 km). Although the distribution of atmospheric water vapor is highly variable in both time and location, its measurement is very important for understanding the Earth's water cycle, greenhouse effect, and weather phenomena (refs. 1 and 2).

The water cycle involves interactions among the Earth's global systems; the atmosphere, hydrosphere, cryosphere, lithosphere, and biosphere. Water is considered the main media for energy transfer between most of these systems. Although the amount of atmospheric water vapor represents only a small percent of the Earth's water reservoir, it is very dynamic and its latent heat transformation is considered the main energy source that maintains the atmospheric general circulation (refs. 1 and 2).

Water vapor and clouds affect the incident solar radiation by reflecting solar radiation back to space and also absorbing some of this energy within the atmosphere, which substantially moderates the Earth's climate. On the other hand, water vapor and clouds affect infrared radiation released by the Earth's surface. Some of this radiation is reflected back to the surface and some is absorbed and reemitted at a lower temperature which contributes to the global warming problem or greenhouse effect (ref. 2).

Water vapor has a direct role in most weather phenomena and natural disasters such as hurricanes. The latent heat of water vapor was found to be the main energy source for hurricanes (ref. 3). The measurement of water vapor flow into a hurricane associated with other observations aids in estimating the

hurricane direction and strength (ref. 3). Therefore, the interest in measuring atmospheric water vapor has increased and leads to developing various techniques to accurately measure its density.

1.1. Water Vapor Measurement

Several techniques are used to measure atmospheric water vapor such as balloon radiosondes, aircraft in situ, and ground- or aircraft-based laser remote sensing. For global measurement of the distribution of water vapor, the most effective method is space-based laser remote sensing. A future goal is to apply laser remote sensing on a space-based platform to continuously measure the water vapor density of the Earth (ref. 4).

Laser remote sensing is a technique used for measuring a molecular density without any physical contact between the sensing device and the atmospheric molecule under observation. It is basically used for applications where direct measurement is very difficult to achieve because of large distances. The technique usually is reliable and fast and does not disturb the measured quantity. Two main classes of laser remote sensing systems are routinely used. One uses the Raman technique and the other uses differential absorption lidar (DIAL) (ref. 4). In the Raman technique, the laser radiation is scattered inelastically from the observed molecule with a frequency shift characteristic of the molecule. The disadvantage of this technique is the complexity of the Raman spectrum. The DIAL technique is more typically used because it is a relatively simpler measurement with higher accuracy (refs. 4, 5, and 6).

1.2. DIAL Technique for Measuring Water Vapor

Light detection and ranging (lidar) is an active remote sensing technique which uses a pulsed laser and a colocated receiver to measure the density of atmospheric gases and aerosols as a function of range. In the DIAL technique, two laser pulses at slightly different wavelengths are transmitted into the atmosphere. The transmitted laser pulses are subjected to scattering and absorption because of the molecules and particles in the atmosphere; therefore, the light backscattered to a telescope receiver contains some information about these molecules and particles which can be evaluated by using the lidar equation (refs. 4, 6, 7, and 8).

When looking at the lidar signals in terms of the received power and if the transmitted laser pulse has an initial optical power P_o, the backscattered received power from a range r is given by (refs. 7 and 8)

$$P(r) = P_o \frac{c\tau A\eta\beta(r)}{2r^2} \exp\left\{-2\int_0^r [\sigma n(r) + k(r)]\, dr\right\} \tag{1}$$

where c is the speed of light, τ is the laser pulse duration, A is the receiver area, η is the receiver efficiency, $\beta(r)$ is the atmospheric volume backscatter coefficient, σ is the absorption cross section of the molecular species of interest, $n(r)$ is the number density profile of the gas, and $k(r)$ is the atmospheric extinction coefficient resulting from all other attenuation processes.

Because the absorption profile of a gas is a unique function of the wavelength, the DIAL technique can distinguish and monitor different atmospheric gases including water vapor. In a water vapor DIAL system, two laser pulses are transmitted through the atmosphere. The wavelength of the first pulse is tuned to the peak of a water vapor absorption line and is called the on-line pulse, whereas the other pulse wavelength is adjusted to a wavelength which corresponds to no absorption and is called the off-line pulse as shown conceptually in figure 1. Because the two wavelengths are so close, the scattering

by atmospheric molecules and particles is essentially equal for both wavelengths, and the difference in the attenuation with range of the return signal is entirely due to the absorption by the water vapor molecules. Thus, the ratio of the backscatter signal at the two wavelengths as a function of range can be used to calculate the water vapor concentration profile (refs. 4, 7, and 8).

Using equation (1) to form a ratio of the on- and off-power returns allows the ability to measure water vapor as a function of range. If the wavelength difference between the on-line and the off-line signals is less than 0.1 nm, $\beta_{on}(r) = \beta_{off}(r)$ and $k_{on}(r) = k_{off}(r)$ can be assumed, and the number density profile of water vapor can be solved as

$$n(r) = \frac{1}{2(r_2 - r_1)(\sigma_{on} - \sigma_{off})} \ln\left[\frac{P_{off}(r_2)\, P_{on}(r_1)}{P_{off}(r_1)\, P_{on}(r_2)}\right] \tag{2}$$

where $r_2 - r_1$ is the range cell for the average concentration, $\sigma_{on} - \sigma_{off}$ is the differential absorption cross section for the two wavelengths, P_{on} is the power received from range r for the on-line wavelength, and P_{off} is the power received from range r for the off-line wavelength. One can then convert the number density profile to a mass mixing ratio by dividing the gas number density by the ambient atmospheric number density (refs. 4, 7, and 8).

2. Background

A critical component in any remote sensing technique is the detector. Water vapor DIAL detection systems typically use avalanche photodiodes (APD's). Compared with a photomultiplier tube (PMT), an APD is much more compact, lightweight, and mechanically rugged and has a lower bias voltage which is suitable for compact size detection systems. Also, an APD has higher quantum efficiency close to 90 percent at wavelengths of 720, 820, and 940 nm, which are water vapor DIAL absorption bands of interest where PMT quantum efficiency is usually very low. APD's typically use a lower bias voltage (hundred of volts) than is required for a PMT (kilovolt range) (refs. 9 and 10).

Compared with p-i-n photodiodes, APD's include an internal gain mechanism which increases their signal-to-noise ratio (SNR). APD's have excellent linearity with respect to incident light intensity. With some structures, an APD can have very low noise in the range of a few $fW/Hz^{1/2}$. For these reasons, water vapor DIAL detection systems use APD's to measure the backscattered light signals (refs. 10 to 13).

2.1. Lidar Atmospheric Sensing Experiment

The lidar atmospheric sensing experiment (LASE) is shown in the block diagram of figure 2. LASE is an instrument that detects water vapor by using the 815-nm water vapor absorption line. LASE measurements were found to have an accuracy better than 6 percent or 0.01 g/kg, whichever is greater across the entire troposphere (refs. 14 and 15).

The LASE transmitter was designed to generate two laser pulses of 30 ns duration each separated by 400 μs at a frequency of 5 Hz with a pulse energy output of 150 mJ. A Ti:sapphire ($Ti:Al_2O_3$) power oscillator was constructed with an Nd:YAG laser as the pump source. Narrow line width and wavelength tuning of the $Ti:Al_2O_3$ laser is achieved by a continuous-wave 100-mW single mode diode laser performing as an injection seed source. This injected seeding allows control of the spectral line width to within 1 pm and provides wavelength tuning stability to ±0.25 pm. The diode laser wavelength is locked

onto the selected water absorption line and tuned by passing a fraction of its frequency modulated light through a reference cell filled with water vapor and detecting the cell transmission. The tunable diode laser seeds the pulsed laser alternately between the on-line wavelength, located at the center of the water vapor absorption line, and the off-line wavelength, typically located 20 to 80 pm away from the on-line wavelength (ref. 14).

The LASE receiver has a Cassegrain telescope with a 40-cm-diameter collecting area. The received light is split into two channels. The two data channels use silicon APD's to increase the measurement dynamic range. The first low-gain channel uses 12 percent of the collected light for measuring strong return signals, whereas the second high-gain APD channel uses 88 percent for low signal level detection. The APD detectors for both channels were EG&G C30955E RT's (reach-through structures) with a 1.5-mm-diameter active area (ref. 14).

The APD detector output signal is applied to a transimpedance amplifier stage which limits the signal bandwidth to 2.5 MHz. A 1.5-MHz low-pass filter is used to set the signal bandwidth, then the signals are applied to 12-bit, 10-MHz digitizers. Both the amplifier and the digitizer stages are mounted in a CAMAC (computer automated measurements and control) crate which communicates with an onboard computer for data recording. The whole system is synchronized by a time-based generated trigger signal (ref. 14).

Although LASE has performed well, several improvements especially in the detection system could be made to reduce system mass and improve performance. Eliminating the CAMAC crate would reduce the system mass substantially and using advanced APD technology could reduce the system noise; thus, the measurement range would be improved (ref. 16).

2.2. DIAL Detection System Development

The main goal of this research is to increase the signal-to-noise ratio of the water vapor DIAL detection system by a factor of 10 compared with the current LASE detection system. Also, the system must be compact in size suitable for placing it directly on the receiver telescope. These goals are achievable with state-of-the-art electronic components, a newly evaluated very low noise APD detector, and the construction of a 14-bit, 10-MHz waveform digitizer, which will be placed as close as possible to this detector (refs. 17 to 20). The new DIAL receiver system is shown schematically in figure 3. The analog circuit will condition the APD output signal and also control its bias voltage and temperature; the digital circuit will convert the analog signal into a digital form. The basis for the APD selection is discussed.

3. Avalanche Photodiodes

APD's are solid state quantum detectors suitable for low light detection in the visible and near infrared regions. These devices are commercially available from many manufacturers and are fabricated with different solid state structures. They have several applications including backscatter lidar, DIAL, and fiber-optic communication. Although they are widely used, few papers in the literature have discussed their characterization.

3.1. APD Structure and Theory of Operation

The basic structures of a p-i-n diode and three other APD's and their electric field distribution are shown in figure 4. The p-i-n diode shown in figure 4(a) is a p-n junction with an intrinsic or lightly doped layer sandwiched between the p and n layers. This structure serves to extend the width of the

depletion region which increases the volume available for absorbing the incident photons. Also it reduces the junction capacitance; thereby, the RC time constant is reduced, which results in higher detection bandwidth. Thus the response time of these devices is in the range of tens of picoseconds, which corresponds to bandwidths of gigahertz (refs. 10 to 13). A disadvantage of p-i-n detectors is that they have no internal gain mechanism. The APD structure, similar to the p-i-n diode structure, has a gain mechanism within the device called the impact ionization process in which the photoelectric charge carriers, because of their high energy, can impact and cause ionization of lattice atoms leading to an avalanche breakdown or internal gain (refs. 10 to 13 and 21).

As shown in figure 4(b) the beveled-edge APD has the simplest structure of the ones used. It consists of a p^+-n junction with a high resistivity n layer which increases the breakdown voltage of the device into the range of kilovolts. Breakdown at the edges is prevented by beveling and making the junction very deep in the range of 50 μm. Therefore, the dead part of the p^+ layer is usually etched away to reduce the device depth. Because the n layer is much deeper than the p^+ layer, electrons produced there are more likely to be multiplied than holes. This reduces the dark-current noise which is mostly generated by hole current. The disadvantage, however, is that only light absorbed in the p layer leads to effective multiplication, and this layer has the lowest electric field. Therefore, charge accumulates slowly, which leads to a longer response time typically in the range of tens of nanoseconds (ref. 21).

The reach-through structure APD with its electric field distribution is shown in figure 4(c). This structure consists of an absorption region and, separated from it, a multiplication region. In the absorption region, the p^+ layer at the active surface is followed by an intrinsic wide layer, which increases the photon absorption depth. The emitted photoelectrons drift and reach a constant velocity. In the multiplication region, the p-n^+ layers form a thin junction with a high internal field, which enhances the impact ionization process (refs. 21, 22, and 23). Recently, an enhancement of the reach-through structure, known as the "super low ionization ratio κ" (SLIK) geometry, has become available and is shown in figure 4(d) (ref. 24). The ability of electrons and holes to "impact ionize" to generate additional charge carriers is characterized by the ionization coefficients α and β for electrons and holes, respectively. The ionization coefficient represents the ionization probabilities per unit length. An important parameter is the ionization ratio κ given by

$$\kappa = \frac{\beta}{\alpha} \tag{3}$$

In APD's, it is desirable to reduce κ as much as possible so that the multiplication process is only due to electrons, since hole current leads to high dark-current noise (ref. 10). This reduction was achieved in the SLIK structure by increasing the absorption region electric field and merging this region with the multiplication region (ref. 24). Typically, the value of κ is in the range of 0.02 for the reach-through structure, whereas it is 0.002 for the SLIK structure (ref. 24). The structure types and the manufacturer's data for the characterized APD's are given in appendix A.

3.2. APD Characteristics and Applied Circuit

An APD with no incident light has *V-I* characteristics similar to a rectifier diode as shown theoretically in figure 5(a). However, when the device absorbs photons due to incident light, the characteristics will be shifted downward. Fortunately, this shift is highly linear with the intensity of the absorbed light.

Furthermore, the new shifted curves are parallel with the original curves as shown in figure 5(b). The *V-I* relation of the device can be given by (refs. 10 and 11)

$$I = I_s\left(e^{qV/kT} - 1\right) - I_d \tag{4}$$

where I is the current through the device, I_s is the saturation current, q is the electron charge, V is the applied voltage, k is the Boltzmann constant, and T is the temperature. Equation (4) resembles the diode equation with the first term representing the dark current and the additional term I_d representing the photocurrent given by (refs. 10 and 11)

$$I_d = \eta G \frac{q}{hc} \lambda P \tag{5}$$

where η is the quantum efficiency, G is the APD internal gain, h is Planck constant, c is the light speed in vacuum, λ is the incident light wavelength, and P is the incident optical power. By knowing the APD sensitive area A, the optical power can be related to the light intensity I (W/m^2) by

$$P = IA \tag{6}$$

By definition the detector responsivity $\Re$ (A/W) can be obtained from equation (5) and is defined by (refs. 10 and 11)

$$\Re = \frac{I_d}{P} = \eta G \frac{q}{hc} \lambda \tag{7}$$

Because APD's can source current through the internal photoeffect, they may operate without the need of an external power source. However, speed of response and gain can be improved by using an externally applied bias voltage. Thus, in most applications an external reverse voltage bias is applied to the APD. The APD current variation, representing the change in the light intensity, is then converted to a voltage variation by a current-to-voltage converter or transimpedance amplifier (TIA). This configuration is shown in figure 6 where R_f is the amplifier feedback resistance, and R and C act as a low-pass filter which eliminates any bias voltage ripple noise. A disadvantage of this technique is the additional noise associated with the TIA as well as the limitation in the frequency response (refs. 10 and 25).

4. Responsivity Calibration

The APD spectral response was measured over a wavelength range from 600 to 1100 nm by comparison with a reference detector calibrated by the NIST (National Institute of Standards and Technology. (See appendix B.) Each detector was placed in the same uniform light field at the same position; this allowed the APD's to be calibrated at certain wavelengths in the specified range. Because the APD response is dependent on its bias voltage and temperature, both dependencies were characterized relative to the reference detector and were maintained constant during the calibration. At each wavelength, the test APD responsivity $\Re_d$ was calculated by substituting equation (6) into (7) to obtain

$$\Re_d = \frac{I_d}{IA_d} \tag{8}$$

where I_d and A_d are the test APD output current and sensitive area, respectively, and I is the intensity of the uniform field. The light intensity can be obtained from

$$\mathrm{I} = \frac{I_r}{\Re_r A_r} \tag{9}$$

where I_r is the reference detector output current, A_r is the sensitive area, and $\Re_r$ is the responsivity at the same wavelength. Combining equations (8) and (9) gives

$$\Re_d = \frac{I_d}{I_r}\frac{A_r}{A_d}\Re_r \tag{10}$$

Furthermore, the test and reference detector output currents were determined by dividing the feedback resistance into the measured voltage output of a TIA. Substituting this result into equation (10) results in

$$\Re_d = \frac{V_d}{V_r}\frac{R_r}{R_d}\frac{A_r}{A_d}\Re_r \tag{11}$$

where R_r and R_d are the feedback resistances for the reference and test detectors, respectively, and V_r and V_d are the TIA output voltages for the reference and test detectors, respectively.

As indicated from equation (4), the APD output signal is associated with a dc offset due to its dark current. Another offset is also added due to the background and thermal radiation. A good practice in such experiments is to use an optical chopper to modulate the input light signal to the detector. The dc offsets can then be eliminated with a high-pass filter at the APD output. This technique allows one to measure very small photocurrents in a range of nanoamperes with sensitive instruments such as lock-in amplifiers. In this case, the chopping factor CF must be considered for correcting the APD output reading obtained from this instrument $V_{\text{lock in}}$ to its peak-to-peak value $V_{p\text{-}p}$ which is the true indication of the light intensity. Thus, the chopping factor is given by

$$\mathrm{CF} = \frac{V_{\text{lock in}}}{V_{p\text{-}p}} \tag{12}$$

Because of ac coupling, the operating frequency of the chopper is chosen to maximize the output signal. The typical chopped output response and that of the ideal square wave response are shown in figure 7(a). A good practice is to obtain the variation of the chopping factor against the chopping frequency as shown in figure 7(b). For this particular case, the chopping factor was maximized at frequencies above 700 Hz.

If CF_r and CF_d are the chopping factors for the reference and test detectors, respectively, equation (11) can be modified to

$$\Re_d = \frac{(V_d)_{\text{lock in}}}{(V_r)_{\text{lock in}}}\frac{\mathrm{CF}_r}{\mathrm{CF}_d}\frac{R_r}{R_d}\frac{A_r}{A_d}\Re_r \tag{13}$$

Equation (13) was used for absolute calibration of the tested APD's in terms of the calibrated reference detector.

4.1. Experimental Setup

The experimental setup for the APD responsivity calibration is shown in figure 8. The light source was a halogen lamp supplied by a stabilized power supply to ensure a stable spectrum and intensity. The lamp output was filtered by a 600-nm high-pass filter to prevent higher order dispersion of shorter wavelengths from being collected in first-order dispersion in the range of 600 to 1100 nm. The chopper was used to modulate the optical signal. For most of the APD's, a 200-Hz chopping frequency was sufficient to optimize the chopping factor. The monochromator was used to separate the light input into its spectral components. An integrating sphere was used to diffuse the exiting light to ensure intensity uniformity at the detector, which is especially important for large area detectors. A disadvantage of using the integrating sphere is the considerable reduction in light intensity. For small area detectors, where a higher intensity was required, the integrating sphere was replaced by a diffuser; or in some cases, the light was applied directly to the detector. For these cases, the field intensity was measured to determine its uniformity.

The APD output was filtered by a high-pass filter to eliminate any dc offsets, as discussed in section 2. An oscilloscope was used to check the detected signal and to obtain its peak-to-peak value, and a lock-in amplifier was used to measure the signal root-mean-square (rms) value.

The test detector was placed on an electrical board and put inside a cooling chamber (appendix C). The chamber was located on a three-axis translation stage for alignment purposes. A temperature controller and a thermoelectric cooler (TEC) were used to fix the temperature of the APD under test. This temperature was measured with a temperature sensor and a digital voltmeter. A stable high-voltage supply biased the APD, and a ±15-V power supply was used to bias the TIA.

The chopper controller adjusted the chopping frequency and supplied synchronization signals for the other instruments. A personal computer sent commands to the monochromator to adjust the grating position that sets the wavelength for the spectral scan, and it acquired the lock-in amplifier and the temperature readings with a GPIB data acquisition card. Appendix B gives the model numbers, manufactures, and descriptions of the instruments used in this setup.

4.2. Experimental Procedure

The reference and test detectors required accurate positioning because the output of the integrating sphere, diffuser, and the light source have intensities that decrease by the inverse of the square of the distance between the source and the detector. The distance between the light outlet and the detector active area was 75 to 150 mm. A microscope with a depth of focus measured to be 200 μm was used to position both detectors as shown in figure 9. Applying the inverted square function, the worst case deviation of the intensity at the detector was ±0.53 percent. Errors due to positioning of the detectors will cause absolute calibration uncertainty of less than 1 percent. The microscope was placed on a kinematic mount (1 μm placement precision) so that it could be removed from the optical path and precisely replaced in the path for detector positioning.

The monochromator was set at 690 nm, because the halogen spectral output was a maximum at this value, and the chopping factor and measurement system range were determined for both the reference and test detectors. The slits of the monochromator were adjusted to have a wavelength band pass of 10 nm.

4.3. Data Analysis and Results

The results from the measurements were analyzed with the Mathworks MATLAB software. The MATLAB software uses vector and array processing that simplifies the analysis of large repetitive data sets. (See appendix D.) By referring to equation (13), we can define a normalized calibration vector {cal} given by

$$\{\text{cal}\} = \frac{\{\Re_r(\lambda)\}}{\{(V_r)_{\text{lock in}}(\lambda)\}} \frac{R_r}{R_d} \frac{A_r}{A_d} \text{CF}_r \tag{14}$$

This vector was calculated for each APD and used for converting its output voltage variation, measured by the lock-in amplifier, into a responsivity variation with respect to wavelength.

The spectral response of the test detectors is shown in figure 10. To compare the results with the manufacturer data sheets, room temperature and manufacturer-specified bias voltage were used as indicated in the figure. The responsivity at wavelengths of interest to water vapor DIAL measurements are also given. In some detectors with a built-in TIA, the value of the feedback resistance was unknown, and the responsivity was given in V/W.

According to equation (7), the APD responsivity is directly proportional to the wavelength of the incident light; this is true, as indicated in figure 10, for wavelengths starting at 600 nm up to the point where the response begins to roll off. Ideally, the roll-off point would be sharp and correspond to the energy bandgap of silicon which is 1000 nm. At this cutoff wavelength, the responsivity decreases sharply because of insufficient energy in the incident photons for the generated electrons to overcome the energy bandgap; this results in a reduction of the APD quantum efficiency. The deviation from the ideal cutoff found in our characterized APD's was mainly due to charge collection inefficiency of photons outside the depletion region of the APD, which was dependent on the type and level of the doping materials used to manufacture the device (refs. 10, 21, and 23).

5. Temperature Dependent Responsivity

At fixed bias voltage and wavelength, the responsivity of an APD detector increases with decreasing temperature. Low temperature operation of an APD leads to an increased output signal due to the increase in the responsivity and also a decreased noise level due to the reduction of the dark current. This low temperature operation results in an increased signal-to-noise ratio (refs. 10, 11, 26, and 27).

This experiment investigates the effect of temperature on the APD spectral response. Empirical relationships for the responsivity versus temperature were determined at the water vapor absorption lines near wavelengths of 720, 820, and 940 nm. Parasitic heat load from the electronics and a nitrogen gas purge allowed the APD operating temperature to be adjusted from near 0°C up to room temperature (appendix C). The nitrogen gas flow was used to avoid condensation and icing inside the cooling chamber. Remember that a lower operating temperature causes the detector breakdown voltage to also decrease. Therefore, this bias must be chosen carefully while performing this test to avoid destroying the APD.

5.1. Experimental Procedure

The responsivity calibration setup, shown in figure 8, was used in this experiment but only for the test detectors. During the experiment, the detector bias voltage was kept constant to ensure that the

spectral response variation is only due to changes in temperature. To avoid detector saturation, the bias voltage was maintained at 5 percent lower than the manufacturer-specified value. Using the alignment setup shown in figure 9, the detector position with respect to the light source was adjusted to the same value used for the responsivity calibration experiment to ensure the same input light intensity.

The temperature controller shown in figure 8 fixed the operating point for each spectral scan. For each temperature set point, the system was allowed to reach equilibrium before proceeding with the experiment. This whole procedure was repeated for each APD under investigation.

5.2. Data Analysis and Results

For each APD, the following characterization results are presented:

1. The APD detector output voltage variation with wavelength $\{V_n(\lambda)\}$

2. The APD temperature variation with wavelength $\{T_n(\lambda)\}$

Ideally, the temperature should be constant with respect to wavelength. This relationship was not true in our investigation because of some deficiencies in the temperature controller used in the experiment. Therefore, the temperature had to be recorded for each wavelength increment $\{T_n(\lambda)\}$. To obtain the APD temperature T_n, this data set was averaged according to

$$T_n = \overline{\{T_n(\lambda)\}} \tag{15}$$

At the same temperature T_n and using equation (14), the detector output voltage variation was converted to a responsivity variation with respect to wavelength according to the relation

$$\{\Re_n(\lambda)\} = \frac{\{V_n(\lambda)\}}{\mathrm{CF}_n}\{\mathrm{cal}\} \tag{16}$$

This procedure was repeated for every temperature setting giving the spectral response variation with temperature shown in figure 11 for all APD's.

Again we used MATLAB software to analyze the results because of its ability to efficiently handle vector and matrix operations. A responsivity vector $\{\Re(T)\}$ and a temperature vector $\{T\}$ were constructed, at a certain wavelength λ_x, as shown in the following equations:

$$\{\Re(T)\} = \{\Re_1(\lambda_x) \quad \Re_2(\lambda_x) \quad \ldots \quad \Re_n(\lambda_x) \quad \ldots \quad \Re_N(\lambda_x)\} \tag{17}$$

$$\{T\} = \{T_1 \quad T_2 \quad \ldots \quad T_n \quad \ldots \quad T_N\} \tag{18}$$

When applying a polynomial curve fit, the responsivity variation with temperature at λ_x took the form

$$\Re(T)|_{\lambda_x} = \sum_{m=0}^{M} a_m T^m \tag{19}$$

where M is the curve fit order and N in equation (18) is the index for maximum temperature. The responsivity versus temperature for all APD's at the water vapor DIAL wavelengths of interest is shown in figure 11. Table 1 gives the curve fitting results and conditions for each APD.

The responsivity with respect to the temperature relationship allowed us to determine the optimum APD operating temperature for the future DIAL detection system. It also determined the control temperature stability requirements. As an example, let us assume APD12 is the chosen detector, and it will operate at 820 nm with 336 V and 0°C. The responsivity derivative (table 1) with respect to temperature is given by

$$\left.\frac{\partial \Re(T)}{\partial T}\right|_{\lambda_x=820} = -8.23 + 0.82T - 23.7 \times 10^{-3} T^2 \tag{20}$$

Thus, a temperature deviation of $\Delta T = 0.1°C$, near $T = 0°C$, results in a responsivity deviation of $\Delta\Re = -0.823$ A/W with a relative error $\Delta\Re/\Re = -0.72$ percent. Thus, the temperature controller and heat sinking requirements were established for the design of the final detection system.

6. Bias Voltage Dependent Responsivity

At fixed temperature and wavelength, the responsivity of an APD increases with increasing bias voltage up to the breakdown voltage. This increase in responsivity is due to the increase of the internal electric field leading to the transfer of more energy to the photocharge carriers, which enhances the impact ionization process. Bias voltages above breakdown cause rapid charge carrier generation which usually leads to device damage if applied for long periods of time (refs. 21, 23, and 24). This experiment investigates the effect of the APD bias voltage variation on the spectral response of interest and obtains responsivity versus bias voltage relations at the water vapor DIAL wavelengths.

6.1. Experimental Procedure

Similar to the previous experiment, the responsivity calibration setup was used only for the test APD's. During the experiment, the APD temperature was kept constant at room temperature to ensure that the spectral response variation is only due to the bias voltage. The detector position with respect to the light source was adjusted to the same value as for the responsivity calibration experiment to ensure the same light intensity input.

With the high-voltage supply shown in figure 8, the detector bias is set to a certain value, and the temperature was stabilized by the controller to room temperature. The output peak-to-peak voltage was then measured with the oscilloscope, and its rms value was measured with the lock-in amplifier in order to calculate the chopping factor. Next, the wavelength was scanned from 600 to 1100 nm with a step increment of 10 nm. For each step increment, the wavelength, output voltage, and temperature were recorded with the computer. Finally, the experiment was repeated for a set of different bias voltages. This procedure was repeated for each APD under investigation.

6.2. Data Analysis and Results

At the end of this experiment, each APD had a group of data files describing its output voltage variation with wavelength at a given bias voltage. The data analysis was performed once again by using MATLAB software. The value of the bias voltage V_{B_n} was measured directly from the high-voltage supply. For a certain APD at a given bias voltage, the available data were as follows:

The APD detector output voltage variation with wavelength $\{V_n(\lambda)\}$

The APD temperature variation with wavelength $\{T_n(\lambda)\}$

Similarly, the temperature data were averaged by using equation (15), and the detector output voltage variation was converted to a responsivity variation with respect to wavelength according to equation (16). This procedure was repeated for every bias voltage setting which produced the spectral response variation with bias voltage.

Now, to obtain the responsivity variation with bias voltage at a certain wavelength λ_x, the spectral response variation with bias voltage is used to form two vectors: a responsivity vector $\{\Re(V_B)\}$ and a voltage bias vector $\{V_B\}$, which are

$$\{\Re(V_B)\} = \{\Re_1(\lambda_x) \quad \Re_2(\lambda_x) \quad \ldots \quad \Re_n(\lambda_x) \quad \ldots \quad \Re_N(\lambda_x)\} \tag{21}$$

$$\{V_B\} = \{V_1 \quad V_2 \quad \ldots \quad V_n \quad \ldots \quad V_N\} \tag{22}$$

By using a polynomial curve fit, the responsivity variation with bias voltage is given by

$$\Re(V)|_{\lambda_x} = \sum_{m=0}^{M} a_m V^m \tag{23}$$

where M is the curve fit order and N is the index for maximum voltage bias. This analysis was applied to each APD at wavelengths of 720, 820, and 940 nm.

The experimental results are shown in figure 12. For each detector, the spectral response variation with bias voltage is shown on the set of curves to the left, and the responsivity variation with bias voltage is shown to the right. Table 2 shows the curve fit coefficients and the test conditions for each detector.

The responsivity–bias voltage relation can be used for determining the APD operating bias in the final DIAL detection system, and it gives an error estimate which helps in evaluating the system accuracy. As an example, assume APD12 is the chosen detector, and it operates at 820 nm with a bias voltage of 336 V and a temperature of 25°C. When referring to figure 12(b), we find that any small variation in the bias voltage around 336 V will cause a small variation in its responsivity relative to higher voltage bias, but the value of the responsivity is relatively stable. On the other hand, table 2 shows that the responsivity derivative with respect to bias voltage is given by

$$\left.\frac{\partial \Re(V)}{\partial V}\right|_{\lambda_x=820} = -2.27 \times 10^5 + 2 \times 10^3 V - 6.12 V^2 + 6 \times 10^{-3} V^3 \tag{24}$$

Thus, a bias voltage deviation of $\Delta V = 1$ V near the bias of 336 V bias results in a responsivity deviation of $\Delta\Re = 1.8034$ A/W which will lead to a relative error of $\Delta\Re/\Re = 4$ percent.

7. Responsivity Uniformity Scan

The APD sensitive area can be considered a group of point detectors distributed along the surface. Ideally, this distribution is uniform with each of these detectors having the same responsivity for similar operating conditions, and therefore, the responsivity distribution is constant along the APD surface. Practically, this condition is not true because of defects developed in the APD manufacturing processes.

In this experiment, we investigated the uniformity of APD responsivity across its surface and determined its active area. This measurement required a relatively small-spot-size light source and the ability to scan it across the detector area. Measuring the APD output voltage as a function of light spot position results in a responsivity map of the APD area.

7.1. Experimental Setup and Procedure

The small-spot-size light source was achieved with the setup shown in figure 13. A 633-nm He:Ne laser output was focused by using a microscope objective. The position of the detector was adjusted with a computer-controlled two-dimensional translation stage. The motion of the detector was adjusted so that the focused laser beam spot and the APD sensitive area remained in the same plane. A neutral density filter was used to avoid APD saturation.

The laser focusing optical system was calibrated to determine the displacement between the laser focus at its minimum waist and the visual focus of the microscope system shown in figure 14. In order to obtain this calibration, a pinhole was mounted on a three-dimensional translation stage, as shown in figure 15. The laser focus was determined by positioning the pinhole such that the maximum laser output was observed on the detector. The laser focus was measured with the micrometer on the translation stage. The visual focus was determined by viewing the best focus of the pinhole through the eyepiece. The test detectors were positioned by finding the visual focus of the detector surface and then translating to the laser focus by the calibrated displacement described previously. During the scan sequence the detector moves in a two-dimensional raster scanning sequence with a fixed step size. The data are then plotted and analyzed with MATLAB.

7.2. Data Analysis and Results

The focused laser spot intensity profile was characterized by scanning a 10-μm-diameter hole in the plane of the laser focus. The results of this scan are displayed in figure 16, and the full width half maximum (FWHM) of the laser spot was 8 μm. Table 3 lists the results of each APD active area, percentage nonuniformity, scanned array step format, and the step size. The active area was defined by the FWHM points in the uniformity scans. The nonuniformity is defined by

$$\text{Nonuniformity} = \frac{\text{Std}}{\text{Mean}} 100 \tag{25}$$

where Std and Mean are the standard deviation and the mean of the surface scan data, respectively.

The normalized surface scan results for the tested APD's (three-dimensional plots shown to the left) and the surface images (shown to the right) are shown in figure 17. In the surface images, darker areas represent lower responsivity, whereas brighter areas represent higher responsivity.

For example, figures 17(c) and (d) demonstrate the response variation over the area of APD10. In some DIAL systems, the light intensity is focused on a small region of the detector. Therefore, these surface scan data can be used to calculate the responsivity correction factor because the calibration of the APD, as discussed in section 2, considers the average responsivity over the entire detector active area.

On the other hand, the surface scan data can be used to determine the APD hot spots, which are points on the APD surface with very high responsivity relative to the average as shown, for example, in figure 17(i) for APD7. The hot spots may cause a problem since at high light intensities, the concentration of charge carrier will increase at this position. This concentration leads to an increased power dissipation at this spot, which will possibly result in local damage of the APD area.

8. Noise Measurement

Noise signals can be divided into two kinds: systematic noise and natural device noise. Systematic noise is mainly due to conduction and interference from the wiring associated with the detector and the surrounding instruments (such as power supplies and pulse generators), and it is independent of the detection process. It can be successfully reduced by proper shielding of the connecting wires, grounding, differential measurement technique, or measuring it in dark condition and subtracting it from the detector output with light applied. The natural device noise is fundamental in nature and is mainly due to the operation of the optical detector itself. It is due to random processes and, thus, can be reduced by averaging. The dominant types of natural device noise are the signal-induced shot noise, the dark current shot noise, and the Johnson noise. In this section, we will discuss these dominant natural noise sources associated with APD operation and its TIA circuit and how it can be measured (refs. 10, 11, and 21).

8.1. Types of APD Inherent Noise

The first type of APD inherent noise is signal-induced shot noise. It is generated by the randomness in photon arrival times which leads to fluctuations in the detector output signal. Because of the internal gain in the APD, an additional noise is added to the optical shot noise; this is known as the multiplication gain noise, which is mainly due to the randomness in the impact ionization process. The total shot noise current in this case is given by (refs. 10, 11, 12, 28, and 29)

$$(i_n)^2_{\text{shot}} = 2\eta q^2 B G^2 \frac{P}{hc}\lambda \tag{26}$$

where B is the effective bandwidth of the detector and G is the device internal gain.

The second type of APD noise is the dark current shot noise. The APD dark current is given by the first term in equation (4) which contributes a dc offset to the detected current signal. This dc offset can be reduced by proper filtering or by adding another offset with opposite polarity. The problem with dark current lies in the shot noise it creates which is independent of the operating frequency. The dark current noise can be obtained from (refs. 10, 11, and 12)

$$(i_n)^2_{\text{dark}} = 2q i_{\text{dark}} G B \tag{27}$$

The noise sources described above are independent; therefore the noise powers can be added together. The resulting equivalent noise current I_n of the APD is given by combining the noise currents of each noise source obtained from equations (26) and (27) as

$$I_n = \sqrt{(i_n)^2_{\text{shot}} + (i_n)^2_{\text{dark}}} \tag{28}$$

and the signal-to-noise ratio is given by

$$\frac{S}{N} = \frac{I_d^2}{I_n^2} \tag{29}$$

The noise and signal as a function of the input optical power are shown in figure 18. Only the optical shot noise depends on the input power. The power independent noise is plotted as a straight horizontal line and represents the dark current. The photon shot noise increases as the square root of the optical power. This shot noise power term adds directly to the other noise power of the system. The signal current increases linearly with input power as shown in figure 18. The power at which the signal current equals the total noise current is called the noise equivalent power (NEP), which is the minimum power required to achieve a unity signal-to-noise ratio used to define the detector minimum detectable signal. The NEP (in W/Hz$^{1/2}$) can be evaluated from

$$\text{NEP} = \frac{I_n}{\Re} \tag{30}$$

where I_n is the noise current spectral density in A/Hz$^{1/2}$ and $\Re$ in A/W. Another figure of merit useful in comparing APD's in terms of noise is called the detectivity D^* (in cm-Hz$^{1/2}$/W). This figure of merit is independent of the detector area A and is given by

$$D^* = \frac{\sqrt{A}}{\text{NEP}} \tag{31}$$

An additional noise source introduced to the APD output photocurrent is due to the current-to-voltage conversion process of the TIA. The operational amplifier noise at its output may be considered a combination of the effects of several independent noise sources at its input as shown in figure 19.

The first noise source is the amplifier equivalent noise voltage generator with spectral density e_v (V/Hz$^{1/2}$). The second noise source is the noise voltage generated by the amplifier input current noise flowing through the feedback resistor e_i (V/Hz$^{1/2}$). Usually values for these two noise sources are given in the amplifier data sheet. The last noise source is the Johnson noise e_r (in V/Hz$^{1/2}$) due to the feedback resistance R_f and is given by

$$e_r = \sqrt{\frac{4k_BT}{R_f}} \tag{32}$$

where k_B is Boltzmann constant and T is the temperature in Kelvins. The total noise at the amplifier output is then given by the sum of the individual noise powers plus the APD noise itself as shown in the following equation (ref. 25):

$$E_n = \sqrt{e_v^2 + e_i^2 + e_r^2 + (I_n R_f)^2} \tag{33}$$

8.2. APD Noise Measurement and Results

The APD noise measurements were performed by using a spectrum analyzer with a 1-Hz normalized spectrum at a spectral resolution bandwidth of 10 kHz. Appropriate care was taken to ensure that the detector dark current and preamplifier noise were the dominant noise sources. The measured power spectral noise n (in dBm) was converted to the APD noise current spectral density I_n by the equation

$$I_n = \sqrt{\frac{10^{0.1n} R_L \times 10^{-3}}{G_A R_f}} \tag{34}$$

where R_L is the APD load resistance and G_A is a preamplifier gain. This quantity was observed to be constant over the APD bias voltage and temperature operating range. Table 4 gives the noise current spectral density, NEP, and D^* for the tested detectors at their responsivity calibration bias voltage and temperature.

The results of this experiment are very important since they directly indicated that APD12 and APD11 were the best detectors for the water vapor DIAL detection system; APD2 represents the detector that is currently used in the LASE detection system.

The APD excess noise factor F as a function of its gain G and ionization ratio κ is given by (refs. 29, 30, and 31)

$$F = \kappa G + (1 - \kappa)\left(2 - \frac{1}{G}\right) \tag{35}$$

For SLIK APD's, APD12 and APD11, the gain is in the range of 500, whereas for a reach-through structure, such as APD2, the gain is 150. Substituting the gain and the ionization factor values given in section 1.2, we find that the SLIK structure has a 40-percent reduction in the excess noise factor over the reach-through structure. A quick comparison (table 4) agrees with this statement and indicates the lower noise content of APD12 and APD11, which helps in achieving our goal of increasing the signal-to-noise ratio of the DIAL detection system by a factor of 10 over the current detection system (APD2).

9. Frequency Response

The frequency response of an APD is determined by the device time response. The time response of an APD is the time interval between the event of photon absorption and the event of photocurrent generation at its output. This time is dependent on the transient time spread, the diffusion time, the RC time constant, and the avalanche buildup time.

Transient time spread is the time interval between photocharge carrier generation and its detection. The charge delivered to the external circuit, contributing to the photocurrent, by carrier motion in the APD material is not provided instantaneously but consumes a time interval because of the drift of the carrier. This time interval is known as the transient time spread. Since holes are much slower than electrons, the transient time spread is dominated by the hole mobility.

Carriers generated outside the depletion region, but sufficiently close to it, take time to diffuse into it. These carriers will contribute to the photocurrent. But since the diffusion is a slow process relative to the drift, it increases the device response time.

The RC time constant in an APD is formed by the equivalent resistance and equivalent capacitance of the device and its circuitry. These elements serve to integrate the output photocurrent of the device leading to increased response time.

The generation of additional charge carriers by the impact ionization process in the multiplication region consumes time, specially if the resulting carriers themselves are causing the generation of more carriers by the same process. This time interval is known as the avalanche buildup time. Since the multiplication is a random process, the avalanche buildup time interval is random and difficult to characterize.

This experiment investigated the responsivity variation of APD12 and APD11 with respect to the frequency of the input signal and the cutoff frequency of the devices to check the manufacturer's stated bandwidth. APD's have a very wide bandwidth on the order of gigahertz, but because of the existence of the built-in TIA in APD12 and APD11, their frequency response is limited by the bandwidth of the internal amplifier which is on the order of megahertz.

9.1. Experiment Setup

The experimental setup for the APD frequency response is shown in figure 20. It consists of a 720-nm laser diode controlled by a pulse generator. The power supply is used to bias the laser diode driver circuit consisting of a buffer amplifier and a voltage-to-current converter. The output laser beam was split to apply part of the optical signal to the reference detector, whereas the other part was applied to the test APD. The reference detector was used to measure the input signal applied to the APD under test. Next, the output of both detectors was measured by a digital oscilloscope and a spectrum analyzer. The function of the oscilloscope was to check the magnitude of the output signal while the spectrum analyzer measured the frequency spectrum. When necessary, a neutral density filter was used to reduce the light intensity to avoid saturating the test APD. The electronic high-pass filter was used to eliminate dc offsets in the detector output.

9.2. Experimental Procedure and Results

With the setup discussed in section 9.1, the APD bias voltage was set to its manufacturer-specified value for room temperature operation. Then, an optical signal was applied to the detectors, after choosing a suitable neutral density filter and checking their output with the oscilloscope. Next, setting the frequency of the input optical signal to a certain value f_i and using the pulse generator, the amplitude of the fundamental frequency components of the APD input and the output signals R_i and C_i, respectively, are recorded in dBm by using the spectrum analyzer. This corresponds to one data point in the frequency domain. By changing the frequency setting of the pulse generator and repeating the same procedures, we obtained the complete frequency scan. Starting from 100 kHz to 1 MHz, we incremented the frequency in 100-kHz steps or from 1 MHz to 20 MHz, a 1-MHz step was used. The spectrum analyzer was set to a frequency range starting at 50 kHz and ending at 20 MHz with each data point averaged 30 times.

Finally, after collecting the data in the frequency range of interest, the analysis was done by using MATLAB. First, the data were stored in three vectors $\{f\}$, $\{C\}$, and $\{R\}$ equivalent to the frequency increments and the corresponding outputs and inputs, respectively. Then, the gain vector $\{G\}$, in dBm, was calculated for each frequency setting from

$$G_i = C_i - R_i \tag{36}$$

The gain-frequency relation was obtained by applying a polynomial curve fit to the gain vector with respect to the frequency vector. By plotting this relation, we can obtain the cutoff frequency from the intersection between the curve and the –3-dB line drawn from the low-frequency gain.

The previous experiment was used to obtain the frequency response for APD12 and APD11 as mentioned. The actual data and the curve fit of the frequency response of APD12 as well as the frequency response of its output and input are shown in figure 21. A similar set of curves is shown in figure 22 for APD11. The measured cutoff frequency of APD12 was 12.75 MHz and for APD11 was 7.8 MHz.

10. Concluding Remarks

In this report, we discussed the characterization of a group of 10 avalanche photodiodes (APD) obtained from three different manufacturers. Each APD was evaluated by calibrating its spectral response, temperature dependent responsivity, voltage dependent responsivity, responsivity uniformity, noise measurements, and frequency response. The results were compared so that a suitable APD detector can be found for advanced water vapor DIAL detection systems. The characterization was focused on two main APD structures, the reach-through structure, which is currently used in the LASE detection system (APD2), and the newer SLIK structure. The SLIK structure APD has better performance because of higher gain and lower noise which leads to an increase in the signal-to-noise ratio of the detection system by at least a factor of 10 over the current system. The SLIK APD package has

1. Built-in, low-noise, transimpedance amplifier

2. Built-in thermoelectric cooler and thermistor for APD temperature control

3. The transimpedance amplifier feedback resistance is cooled along with the detector reducing the Johnson noise

This APD has a small area (0.24 mm^2) compared with the LASE APD (1.7 mm^2), which might produce alignment difficulties. The summary of results for APD11 and APD12 is given in the following table:

APD	Manufacturer, model, serial	λ, nm	d, mm	A, mm^2	Area nonuniformity, percent	V_B, V	T, °C	NEP, $fW/Hz^{1/2}$	ℜ, A/W	D^*, $cm\text{-}Hz^{1/2}/W$	BW (3 dB), MHz
11	EG&G, C30649E, 148	720 820 940	0.556	0.242	14.5	415	0	1.8 1.7 3.1	127.3 133.8 72.3	2.77×10^{13} 2.90×10^{13} 1.57×10^{13}	7.8
12	EG&G, C30649E, 147	720 820 940	0.5	0.24		336	0	1.9 1.9 3.9	113.3 111.2 55.9	2.87×10^{13} 3.05×10^{13} 1.63×10^{13}	12.8

Symbols used in the table are defined as follows:

A area

BW bandwidth

D^* detectivity

d diameter of sensitive area

NEP noise equivalent power

$\Re$ detector responsivity

T temperature

V_B bias voltage

λ wavelength

These characterization experiments provided the basis for the design of an advanced 14-bit atmospheric water vapor detection system, with the APD and its operating parameters indicated in the above table. These detectors represent the best available APD's for the near infrared detection of atmospheric water vapor even with their smaller sensitive area.

Appendix A

APD Manufacturer's Data

The manufacturer's data for the APD's investigated are given in the following table.

Photodiode	Manufacturer	Model, serial	Type (*a*)	d,[b] mm	T,[c] °C	$\Re$[d]	λ,[e] nm	V_B,[f] V	V_{BD},[g] V	I_n/V_n (*h*)	I_d,[i] nA	BW,[j] MHz	NEP,[k] pW/Hz$^{1/2}$
APD12	EG&G	C30649E, 147	SLIK	0.5	25	50 MV/W	820	349	356	150 nV/Hz$^{1/2}$	7	11	0.003
APD11	EG&G	C30649E, 148	SLIK	0.5	25	50 MV/W	820	431	440	150 nV/Hz$^{1/2}$	8	12	0.003
APD10	Electron Tubes, Inc.	SSO-AD-2500, #8-12	RTS	2.52	21.5	45 A/W	880	110	161.7		30	2.2×10^3	0.4
APD9	Electron Tubes, Inc.	SSO-ADH-500, #10	RTS	0.5	21.5	45 A/W	880	150			1.5	1.3×10^3	0.2
APD8	EG&G	C30646E, CD2507	RTS	0.5	22	20 MV/W	850	217	228	78 nV/Hz$^{1/2}$		9.4 M	0.004
APD7	EG&G	C30646E, CD2508	RTS	1.5	22	6 MV/W	1064	384	443	120 nV/Hz$^{1/2}$		9.5 M	0.02
APD6	EG&G	C30659E, CD2472	RTS	0.15		50 MV/W	830	420.4	427	110 nV/Hz$^{1/2}$	36	15	0.002
APD5	Advanced Photonix, Inc.	197-70-71-520	BE	5	22	108A/W	840		2450	2 pA/Hz$^{1/2}$	160	43	0.014
APD4	EG&G	C30950E	RTS	0.8	25	0.52 MV/W	830	275	425	15 nV/Hz$^{1/2}$		50	0.029
APD2	EG&G	C30955E, 1647	RTS	1.5		70 A/W	900	275	390	2 pA/Hz$^{1/2}$	200		

[a]SLIK, super low κ structure; RTS, reach-through structure; BE, beveled-edge structure.
[b]Diameter of sensitive area.
[c]Testing temperature.
[d]APD responsivity.
[e]Testing wavelength.
[f]Bias voltage.
[g]Breakdown voltage.
[h]Spectral noise current (nA/Hz$^{1/2}$) and voltage density (nV/Hz$^{1/2}$).
[i]Dark current.
[j]Bandwidth.
[k]Noise equivalent power.

Appendix B

Characterization Instruments

The reference detector was an ORIEL K7034 detector. It was a p-i-n diode, with a sensitive area of 100 mm^2. The TIA feedback resistor associated with the detector was set to 10^6 Ω. Figure B1 gives the detector spectral response which was used to calibrate all the test APD's.

The test instruments were as follows:

Light source: ORIEL 66181

Optical chopper: ORIEL 75152

Integrating sphere: ORIEL 70451

Temperature controller: Amherst Scientific 7600

High voltage supply: Stanford Research System PS350

Power supply: Hewlet Packard 6234A

Lock-in amplifier: Scitec Instruments

Digital oscilloscope: Hewlett Packard 54601A

Personal computer: Northgate Computer System Inc.

Pulse generator: Hewlett Packard 8116A

Spectrum analyzer: Hewlett Packard 6112A

Laser diode: SHARP LT020MC0

Automatic translation stages: Klinger Scientific MDC3

Monochromator: ORIEL 77200

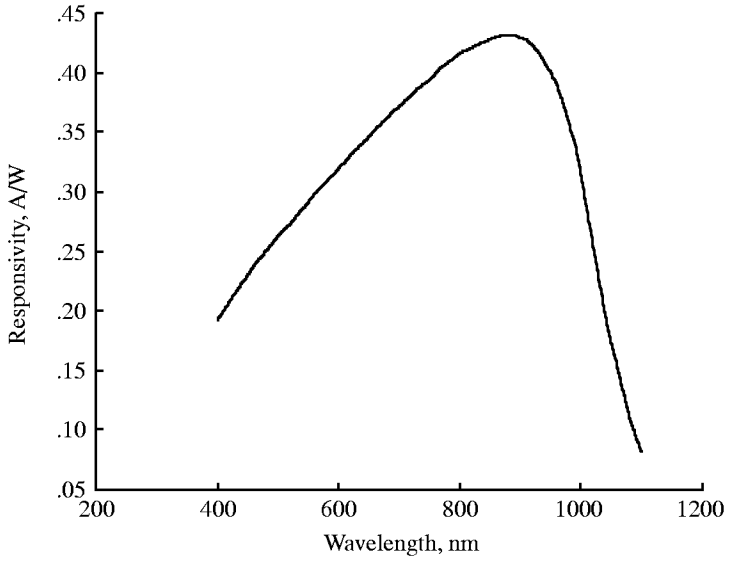

Figure B1. Reference detector spectral response.

Appendix C

APD Test Chamber

A cross section of the APD chamber is shown in figure C1. The chamber is designed to control the environment for detector operation. A thermoelectric cooler is used to cool the detector heat sink. Water circulation is applied to the hot side of the cooler in order to dissipate the heat. The N_2 flow prevents water vapor condensation on the detector window at low temperatures and also avoids dust accumulation inside the chamber.

The detector heat sink is connected mechanically to the cold side of the thermoelectric cooler. The APD's can have different areas; therefore, a mounting ring is used to provide the maximum heat transfer from the detector can to the heat sink, as shown in figure C2. The heat sink design holds the detector as well as a small electronics card (shown in fig. 6). A temperature sensor is located on the heat sink as close as possible to the APD. An experiment was carried out to check the accuracy of the sensor reading with respect to the actual temperature of the detector can, which is assumed to equal the detector temperature itself, by placing another temperature sensor in the detector position as shown in figure C3. The temperature was varied by using the temperature controller for the experimental temperature range. The correction relation between the temperature sensor reading and the APD package temperature is given by

$$\text{Temperature at APD location} = 0.8622 \times (\text{Temperature sensor reading}) + 3.2771$$

The temperature sensor, Texas Instruments model LM35, was a semiconductor sensor. Figure C4 shows the temperature sensor circuit. The output voltage reading in mV was calibrated to give the temperature reading directly.

Another test was performed to examine the transmittance of the chamber window; this was achieved by using APD8 during a responsivity calibration experimental run. The detector output voltage was measured twice with and without the chamber window at the same bias voltage and temperature. The window transmittance is given by

$$\text{Transmittance} = \frac{\text{Output with chamber window}}{\text{Output without chamber window}}$$

The measurement results shown in figure C5 indicate a 0.9844 average widow transmittance across the wavelength range of interest.

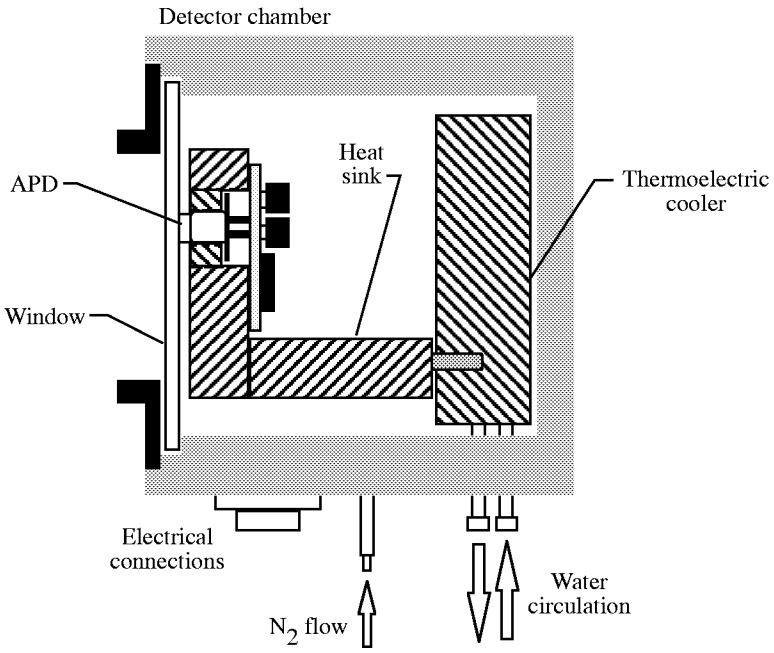

Figure C1. Schematic of APD chamber.

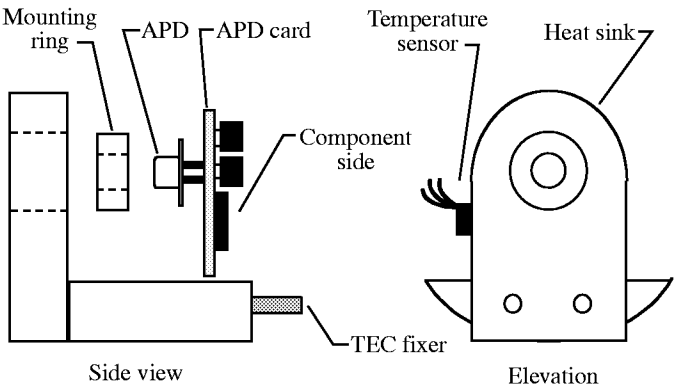

Figure C2. Schematic diagram of APD heat sink.

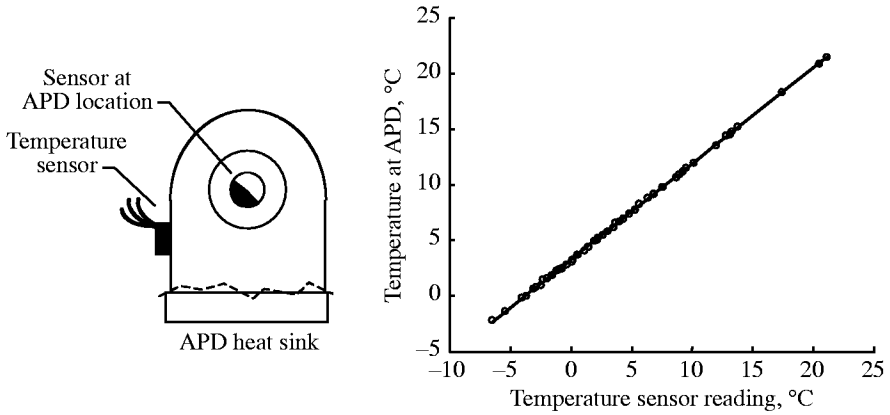

Figure C3. Relation between temperature sensor reading and temperature at APD location.

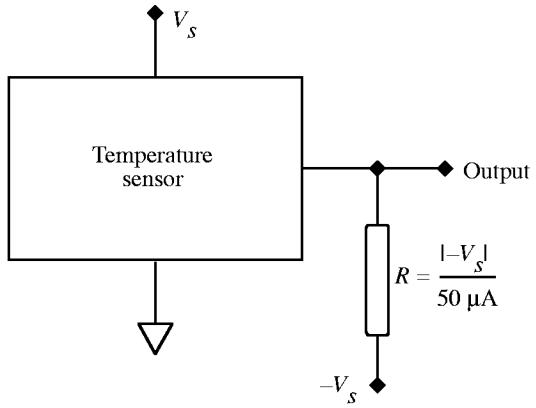

Figure C4. Temperature sensor circuit.

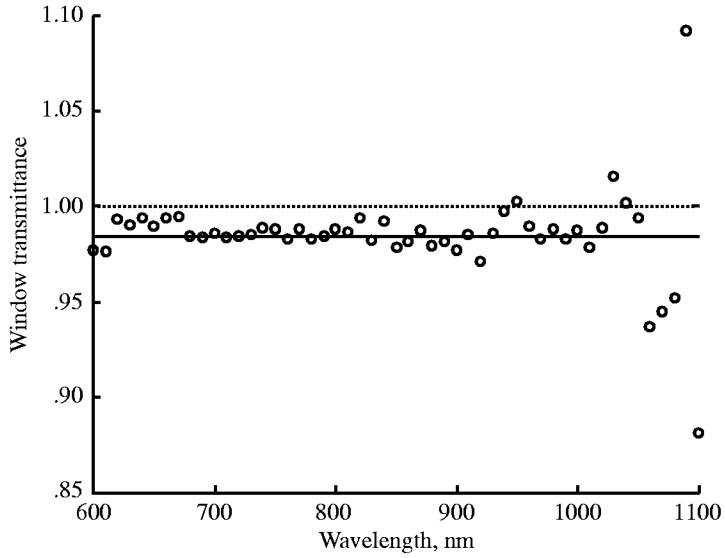

Figure C5. Chamber window transmittance as function of wavelength. Mean window transmittance = 0.9844.

Appendix D

MATLAB Data Analysis Programs

D1. Read Data File Program

The raw data obtained from the APD characterization experiments were in the ASCII format. The Read Data File Program was used to read the raw data files (*filename*) and convert it to a vector format (*vector*) and is given as follows:

```
Function[vector] = read(filename)

fid = fopen(filename,'rt');
if fid < 0
   ret = fid;
   return;
end
vector = zeros([1,41]);
for I = 1:41;
   [a,c] = fscanf(fid,'%f',4);
   vector(I) = a(1);
   if (c ~= 4);
      ret = -1111;
      return;
   end
   status = fseek(fid,0,0);
   if (status < 0)
      if (I == 41)
         fclose(fid);
         ret = 0;
         return
      end
      ret = status;
      return;
   end
end
ret = 0;
fclose(fid);
```

D2. Calibrate Program

The Calibrate Program was used to obtain the calibration results for a certain APD. It reads the wavelength (*wavelength file*), test APD output voltage (*voltage file*), reference detector output voltage (*reference file*), and temperature (*temperature file*) raw data files. The program generates the APD spectral response waveform, the responsivity at the water vapor DIAL wavelengths, and the {cal} vector.

```
[w]  = read(wavelength file);
[vd] = read(voltage file);
[vr] = read(reference file);
[T] = read(temperature file);
```

```
sd = APD output voltage sensitivity
Rd = APD feedback resistance
Ad = APD area
CFd = APD chopping factor
sr = reference detector output voltage sensitivity
Rr = reference detector feedback resistance
Ar = reference detector area
CFr = reference detector chopping factor

load Si_resp.ref;              %Reference Detector Responsivity
for I = 60:110;
Res_r(i-59) = Si_resp(10*I-199,2);
end
m = Rr*Ar*CFr / (Rd*Ad*CFd);
for I = 1:51;
cal(i) = m*Res_r(i)/(vr(i)*sr);
end
vd = sd * vd;
Res_d = cal .* vd;

plot(w,Res_d)
xlabel('Wavelength in nm')
ylabel('Responsivity in A/W')
title('APDxx Spectral Response)
gtext(w(12) Res_d(12))
gtext(w(22) Res_d(22))
gtext(w(34) Res_d(34))
Temperature = mean(T)
```

D3. Temperature Response Program

The Temperature Response Program was used to obtain the spectral response variation with temperature and the responsivity versus temperature variation at the water vapor DIAL wavelengths. It reads the wavelength (*wavelength file*), test APD output voltage (*voltage file*), and temperature (*temperature file*) raw data files.

```
[w]  = read(wavelength file);
[v1] = read(voltage file 1);
[v2] = read(voltage file 2);
.
.
.
[vn] = read(voltage file n);
[T1] = read(temperature file 1);
[T2] = read(temperature file 2);
.
.
.
[Tn] = read(temperature file n);

R1 = sensitivity1 * v1 .* cal;
R2 = sensitivity2 * v2 .* cal;
.
.
.
Rn = sensitivityn * vn .* cal;
figure(1)
plot(w,R1,w,R2,...,w,Rn)
```

```
xlabel('Wavelength in nm')
ylabel('Responsivity in A/W')

temp = [mean(T1) mean(T2) ... mean(Tn)];
Res720 = [R1(13) R2(13) ... Rn(13) ];
Res820 = [R1(23) R2(23) ... Rn(23) ];
Res940 = [R1(35) R2(35) ... Rn(35) ];
[ttemp,rres720,p720,eror720]=fitt(temp,res720,4);
figure(2)
plot(temp,res720,'o',ttemp,rres720)
title(' Temperature Fit at 720nm')
[ttemp,rres820,p820,eror820]=fitt(temp,res820,4);
figure(3)
plot(temp,res820,'o',ttemp,rres820)
title(' Temperature Fit at 820nm')
[ttemp,rres940,p940,eror940]=fitt(temp,res940,4);
figure(4)
plot(temp,res940,'o',ttemp,rres940)
title('Temperature Fit at 940nm')
```

D4. Voltage Bias Response Program

The Voltage Bias Response Program was used to obtain the spectral response variation with voltage bias and the responsivity versus bias variation at the water vapor DIAL wavelengths. It reads the wavelength (*wavelength file*), test APD output voltages (*voltage file*), and temperature (*temperature file*) raw data files.

```
[w] = read(wavelength file);
[v1] = read(voltage file 1);
[v2] = read(voltage file 2);
.
.
.
[vn] = read(voltage file n);
[T] = read(temperature file);

R1 = sensitivity1 * v1 .* cal;
R2 = sensitivity2 * v2 .* cal;
.
.
.
Rn = sensitivityn * vn .* cal;
figure(1)
plot(w,R1,w,R2,...,w,Rn)
xlabel('Wavelength in nm')
ylabel('Responsivity in A/W')

bias = [bias1 bias2 ... biasn];
Res720 = [R1(13) R2(13) ... Rn(13) ];
Res820 = [R1(23) R2(23) ... Rn(23) ];
Res940 = [R1(35) R2(35) ... Rn(35) ];
[vBias,rres720,p720,eror720] = fitt(bias,res720,4);
figure(2)
plot(bias,res720,'o', vBias,rres720)
title('Voltage Bias Fit at 720nm')
[vBias,rres820,p820,eror820] = fitt(bias,res820,4);
```

```
figure(3)
plot(bias,res820,'o', vBias,rres820)
title(' Voltage Bias Fit at 820nm')
[vBias,rres940,p940,eror940]=fitt(bias,res940,4);
figure(4)
plot(bias,res940,'o', vBias,rres940)
title(' Voltage Bias Fit at 940nm')
```

D5. Surface Scan Program

The Surface Scan Program was used to analyze the surface scan data. The inputs to this program include the APD output voltage data (*file*), the background dark current voltage output (*Vbkgd*), the scan step increment array in x-direction (*x*), the scan step increment array in y-direction (*y*), and the translation stage step size for each increment (*step_size*). The program outputs include the position arrays (*xaxis*) and (*yaxis*), the value of the active area (*act_area*), and the responsivity variation along the APD surface.

```
Function [xaxis, yaxis, act_area]= uniform( file, Vbkgd, x, y, step_size);

[dat1] = read(file);
if ( ret < 0 )
   ret = -1;
   sprintf('Input file not read')
   return
end
[I] = mk1dto2d(dat1, x,y);
i1 = min(dat1);
i2 = max(dat1);
d_int = (i2-i1)/256;
if ( I(x / 2,y / 2) > Vbkgd)
   norm=(I - i1)/(i2 - i1);
   end
if ( I(x / 2,y / 2) < Vbkgd)
   norm=(i2 - I)/(i2 - i1);
end
figure(1);
colormap(gray(255));
act_area = 255 * norm;
sel = (act_area > 128);
cnt = 0;
for l = 1:x;
   for m=1:y;
      if(sel(m,l) == 1)
         cnt = cnt + 1;
         lin_area(cnt) = act_area(m,l);
      end;
   end;
end;
if ( cnt == 0)
   ret = -100;
   return;
end;
area = cnt*step_size^2/1e6;
area_ave = mean(lin_area);
```

```
area_std = std(lin_area);
per_area = area_std*100/area_ave;
xaxis = step_size*(1:x);
yaxis = step_size*(1:y);
v = act_area*d_int+i1;
maxv = max(max(v));
minv = min(min(v));
for I = 1:x;
   for j = 1:y;
      v(i,j) = v(i,j)-minv;
      v(i,j) = (100/(maxv-minv))*v(i,j);
   end
end
mesh(xaxis,yaxis,v);
title([file, ': Active Area Response Uniformity ',num2str(per_area),' STD
Percent']);
zlabel('Relative Responsivity');
xlabel('Y-Position in microns');
ylabel('X-Position in microns');
colormap('default');
CM = colormap;
TiffFile = 'name_num.ext';
TiffFile = strrep( TiffFile, 'name', file);
TiffFile = strrep( TiffFile, 'num', '1');
TiffFile = strrep( TiffFile, 'ext', 'tif');
figure(2);
colormap(gray(255));
u = act_area;
maxu = max(max(u));
minu = min(min(u));
image(xaxis,yaxis,u);
title([file, ': Active Area ', num2str(area),' mm^2']);
xlabel('Y-Position in microns');
ylabel('X-Position in microns');
CM = colormap;
axis('square');
TiffFile = 'name_num.ext';
TiffFile = strrep( TiffFile, 'name', file);
TiffFile = strrep( TiffFile, 'num', '2');
TiffFile = strrep( TiffFile, 'ext', 'tif');
```

D6. Frequency Response Program

The Frequency Response Program was used to analyze the frequency response data. For an APD, the raw data are located in three files: the frequency increment (*frequency file*), the reference detector output voltage (*reference file*), and the test APD output voltage (*test file*) files. The output consists of the frequency Bode plots for the APD input, output, and gain.

```
[f]  = read(frequency file);
[r] = read(reference file);
[t] = read(test file);

[p1,s] = polyfit(f,r,2);
rr = polyval(p1,f);
```

```
figure(1)
semilogx(f,r,'o',f,rr)
grid
xlabel('Frequency in Hz')
ylabel('Input in dB')

[p2,s] = polyfit(f,t,2);
tt = polyval(p2,f);
figure(2)
semilogx(f,t,'o',f,tt)
grid
xlabel('Frequency in Hz')
ylabel('Output in dB')

for I = 1:35;
   g(I) = t(I)-r(I);
end
g=g';

figure(3)
[p3,s] = polyfit(f,g,2)
gg = polyval(p3,f);
semilogx(f,g,'o',f,gg)
grid
xlabel('Frequency in Hz')
ylabel('Gain in dB')
```

References

1. Christopherson, Robert W.: *Geosystems: An Introduction to Physical Geography.* Maxwell Macmillan Int., 1992.

2. Starr, D. O'C.; and Melfi, S. H., eds.: *The Role of Water Vapor in Climate—A Strategic Research Plan for the Proposed GEWEX Water Vapor Project (GVaP).* NASA CP-3120, 1991.

3. Zhang, Z.; and Krishnamurti, T. N.: Ensemble Forecasting of Hurricanes Tracks. *Bull. Am. Meteorol. Soc.*, 1997, pp. 2785–2695,

4. Measures, Raymond M.: *Laser Remote Sensing: Fundamentals and Applications.* John Wiley & Sons, Inc., 1984.

5. Whiteman, D. N.; Melfi, S. H.; and Ferrare, R. A.: Raman Lidar System for the Measurement of Water Vapor and Aerosols in the Earth's Atmosphere. *Appl. Opt.*, vol. 31, no. 16, June 1992, pp. 3068–3082.

6. Grant, William B.: Differential Absorption and Raman Lidar for Water Vapor Profile Measurements: A Review. *Opt. Eng.*, vol. 30, no. 1, Jan. 1991, pp. 40–48.

7. Higdon, Noah S.; Browell, Edward V.; Ponsardin, Patrick; Grossmann, Benoist E.; Butler, Carolyn F.; Chyba, Thomas H.; Mayo, M. Neale; Allen, Robert J.; Heuser, Alene W.; Grant, William B.; Ismail, Syed; Mayor, Shane D.; and Carter, Arlen F.: Airborne Differential Absorption Lidar System for Measurements of Atmospheric Water Vapor and Aerosols. *Appl. Opt.*, vol. 33, no. 27, 1994, pp. 6422–6438.

8. Browell, E. V.; Wilkerson, T. D.; and Mcllrath, T. J.: Water Vapor Differential Absorption Lidar Development and Evaluation. *Appl. Opt.*, vol. 18, no. 20, Oct. 1979, pp. 3474–3482.

9. Kume, Hidehiro, ed.: *Photomultiplier Tube—Principle to Application.* Hamamatsu Photonics K.K., 1994.

10. Saleh, Bahaa E. A.; and Tiech, Malvin Carl: *Fundamentals of Photonics.* John Wiley & Sons, Inc., 1991.

11. Dereniak, Eustace L.; and Crowe, Devon G.: *Optical Radiation Detectors.* John Wiley & Sons, Inc., 1984.

12. Agrawal, Govind P.: *Fiber-Optic Communication Systems.* Second ed., John Wiley & Sons, Inc., 1997.

13. Boyd, Robert W.: *Radiometry and the Detection of Optical Radiation.* John Wiley & Sons, Inc., 1983.

14. Moore, Alvah; Brown, Kevin; Hall, William; Barnes, James; Edwards, William; Petway, Larry; Little, Alan; Luck, William; Antill, Charles; Jones, Irby; Browell, Edward; and Ismail, Syed: Development of the Lidar Atmospheric Sensing Experiment (LASE)—An Advanced Airborne DIAL Instrument. *Advances in Atmospheric Remote Sensing With Lidar*, A. Ansmann, R. Neuber, P. Rairoux, and U. Wandinger, eds., Springer, 1997, pp. 281–288.

15. Browell, Edward V.; Ismail, Syed; Hall, William M.; Moore, Alvah S., Jr.; Kooi, Susan A.; Brackett, Vincent G.; Clayton, Marian B.; Barrick, John D. W.; Schmidlin, Frank J.; Higdon, N. Scott; Melfi, S. Harvey; and Whiteman, David N.: LASE Validation Experiment. *Advances in Atmospheric Remote Sensing With Lidar,* A. Ansmann, R. Neuber, P. Rairoux, and U. Wandinger, eds., Springer, 1997, pp. 289–295.

16. DeYoung, R. J.; Halama, G. E.; Luck, W. S.; Eillis, K. S.; Sandford, S. P.; Browell, E. V.; and Refaat, T.: Advanced Detectors, Optics, and Waveform Digitizers for Aircraft DIAL Water Vapor Measurements. *Application of Lidar to Current Atmospheric Topics II*, Arthur J. Sedlacek III and Kenneth W. Fischer, eds., SPIE Vol. 3127, 1997, pp. 103–155.

17. Rafaat, Tamer F.; Luck, William S., Jr.; and DeYoung, Russell J.: Advanced Detector and Waveform Digitizer for Water Vapor DIAL Systems. *Nineteenth International Laser Radar Conference*, Upendra N. Singh, Syed Ismail, and Geary K. Schwemmer, eds., NASA/CP-1998-207671/PT2, 1998, pp. 845–848.

18. Refaat, Tamar F.; Luck, William S., Jr.; and DeYoung, Russell J.: Advanced Water Vapor DIAL Detection System. *Conference on Lasers and Electro-Optics*, IEEE, OSA, May 1999, p. 524.

19. Refaat, Tamer F.; Luck, William S.; and DeYoung, Russell J.: An Advanced Water Vapor Lidar Detection System for Aircraft and Space Deployment. Optical Spectroscopic Techniques and Instrumentation for Atmospheric and Space Research III, Allen M. Larar, ed., SPIE Vol. 3756, 1999, p. 92.

20. Refaat, Tamer F.; Luck, William S., Jr.; and DeYoung, Russell J.: *Design of Advanced Atmospheric Water Vapor Differential Absorption Lidar (DIAL) Detection System*. NASA/TP-1999-209348, 1999.

21. Webb, P. P.; McIntyre, R. J.; and Conradi, J.: Properties of Avalanche Photodiodes. *RCA Rev.*, vol. 35, June 1974, pp. 234–278.

22. *Avalanche Photodiodes: A User's Guide*. EG&G Optoelectronics Canada [1984].

23. McIntyre, R. J.: Recent Developments in Silicon Avalanche Photodiodes. *Measurement*, vol. 13, no. 4, 1989, pp. 146–152.

24. Dautet, Henri; Deschamps, Pierre; Dion, Bruno; MacGregor, Andrew D.; MacSween, Darleene; McIntyre, Robert J.; Trottier, Claude; and Webb, Paul P.: Photon Counting Techniques With Silicon Avalanche Photodiodes. *Appl. Opt.*, vol. 31, no. 21, July 1993, pp. 3894–3900.

25. Clayton, G. B.; and Newby, B. W. G.: *Operational Amplifiers*. Newnes, 1992.

26. Conradi, J.: Temperature Effects in Silicon Avalanche Photodiodes. *Solid State Electron.*, vol. 17, 1974, pp. 99–106.

27. Crowell, C. R.; and Sze, S. M.: Temperature Dependence of Avalanche Multiplication in Semiconductors. *Appl. Phys. Lett.*, vol. 9, no. 6, 1966, pp. 242–244.

28. Van Vliet, K. M.: Noise Limitations in Solid State Photodetectors. *Appl. Opt.*, vol. 6, no. 7, 1967, pp. 1145–1168.

29. Hollenhorst, J. N.: A Theory of Multiplication Noise. *IEEE Trans. Electron Devices*, vol. 37, no. 3, Mar. 1990, pp. 781–788.

30. Redus, R.; and Farrell, R.: *Gain and Noise in Very High Gain Avalanche Photodiodes: Theory and Experiment*. SPIE Vol. 2859, 1996, pp. 288–297.

31. Hakim, N. Z.; Saleh, B. E. A.; and Teich, M. C.: Generalized Excess Noise Factor for Avalanche Photodiodes of Arbitrary Structure. *IEEE Trans. Electron Devices*, vol. 37, no. 3, Mar. 1990, pp. 599–610.

Table 1. Curve Fit of Responsivity Variation With Temperature for Tested APD's

Wavelength, nm	Curve fit equation	Unit
APD12; bias voltage, 336 V; $-3°C < T < 25°C$		
720	$116.3 - 8.69T + 0.43T^2 - (8.3 \times 10^{-3})T^3$	A/W
820	$113.8 - 8.23T + 0.41T^2 - (7.9 \times 10^{-3})T^3$	A/W
940	$57.2 - 3.65T + 0.18T^2 - (3.6 \times 10^{-3})T^3$	A/W
APD11; bias voltage, 415 V; $-3°C < T < 25°C$		
720	$130.02 - 9.63T + 0.45T^2 - (8.3 \times 10^{-3})T^3$	A/W
820	$136.19 - 9.85T + 0.46T^2 - (8.6 \times 10^{-3})T^3$	A/W
940	$73.14 - 4.99T + 0.26T^2 - (4.4 \times 10^{-3})T^3$	A/W
APD10; bias voltage, 110 V; $6.3°C < T < 22.3°C$		
720	$(3.85 \times 10^3) - (9.65 \times 10^2)T + 90.53T^2 - 3.71T^3 + 0.0557T^4$	A/W
820	$(4.22 \times 10^3) - (10.62 \times 10^2)T + 99.88T^2 - 4.09T^3 + 0.0617T^4$	A/W
940	$(2.17 \times 10^3) - (5.47 \times 10^2)T + 51.55T^2 - 2.12T^3 + 0.0319T^4$	A/W
APD9; bias voltage, 150 V; $10.4°C < T < 21.9°C$		
720	$58.9 - 2.92T + (8.82 \times 10^{-2})T^2 - (1.33 \times 10^{-3})T^3$	A/W
820	$66.8 - 3.53T + (9.96 \times 10^{-2})T^2 - (1.15 \times 10^{-3})T^3$	A/W
940	$35.2 - 1.96T + (5.75 \times 10^{-2})T^2 - (6.35 \times 10^{-4})T^3$	A/W
APD8; bias voltage, 190 V; $5°C < T < 23°C$		
720	$(1.5 \times 10^7) - (4.9 \times 10^5)T + (7.6 \times 10^3)T^2$	V/W
820	$(1.6 \times 10^7) - (4.9 \times 10^5)T + (7.58 \times 10^3)T^2$	V/W
940	$(8.95 \times 10^7) - (2.6 \times 10^5)T + (4.2 \times 10^3)T^2$	V/W
APD7; bias voltage, 380 V; $13.3°C < T < 24.5°C$		
720	$(2.24 \times 10^{10}) - (3.26 \times 10^9)T + (1.63 \times 10^8)T^2 - (2.77 \times 10^6)T^3$	V/W
820	$(3.06 \times 10^{10}) - (4.46 \times 10^9)T + (2.24 \times 10^8)T^2 - (3.79 \times 10^6)T^3$	V/W
940	$(3.88 \times 10^{10}) - (5.67 \times 10^9)T + (2.86 \times 10^8)T^2 - (4.85 \times 10^6)T^3$	V/W
APD6; bias voltage, 410 V; $1.1°C < T < 21.9°C$		
720	$(2.91 \times 10^8) - (4.63 \times 10^7)T + (3.07 \times 10^6)T^2 - (6.8 \times 10^4)T^3$	V/W
820	$(2.81 \times 10^8) - (4.53 \times 10^7)T + (3.04 \times 10^6)T^2 - (6.79 \times 10^4)T^3$	V/W
940	$(1.78 \times 10^8) - (2.89 \times 10^7)T + (1.96 \times 10^6)T^2 - (4.4 \times 10^4)T^3$	V/W
APD2; bias voltage, 317 V; $5.7°C < T < 23.1°C$		
720	$928.5 - 189.9T + 17.1T^2 - 0.6985T^3 + 0.011T^4$	A/W
820	$1043.2 - 192.3T + 15.8T^2 - 0.6005T^3 + 0.0086T^4$	A/W
940	$1093.9 - 185.9T + 14.1T^2 - 0.4956T^3 + 0.0066T^4$	A/W

Table 2. Curve Fit of Responsivity Variation With Bias Voltage for Tested APD's

Wavelength, nm	Curve fit equation	Unit
APD12; temperature, 25.0°C; $320 < V < 351$ V		
720	$(1.88 \times 10^7) - (2.25 \times 10^5)V + (1 \times 10^3)V^2 - 2.02V^3 + (2 \times 10^{-3})V^4$	A/W
820	$(1.89 \times 10^7) - (2.27 \times 10^5)V + (1 \times 10^3)V^2 - 2.04V^3 + (1.5 \times 10^{-3})V^4$	A/W
940	$(1.01 \times 10^7) - (1.22 \times 10^5)V + (5.47 \times 10^2)V^2 - 1.09V^3 + (8.2 \times 10^{-4})V^4$	A/W
APD11; temperature, 23.0°C; $390 < V < 430$ V		
720	$-(2.76 \times 10^5) + (2.06 \times 10^3)V - 5.12V^2 + (4.25 \times 10^{-3})V^3$	A/W
820	$-(2.91 \times 10^5) + (2.17 \times 10^3)V - 5.41V^2 + (4.49 \times 10^{-3})V^3$	A/W
940	$-(1.65 \times 10^5) + (1.23 \times 10^3)V - 3.07V^2 + (2.54 \times 10^{-3})V^3$	A/W
APD10; temperature, 20.9°C; $80 < V < 115$ V		
720	$-(9.1 \times 10^3) + 296.7V - 3.19V^2 + (1.14 \times 10^{-2})V^3$	A/W
820	$-(9.5 \times 10^3) + 308.6V - 3.32V^2 + (1.19 \times 10^{-2})V^3$	A/W
940	$-(5.2 \times 10^3) + 167.7V - 1.81V^2 + (6.46 \times 10^{-3})V^3$	A/W
APD9; temperature, 22.0°C; $125 < V < 150$ V		
720	$-(3.2 \times 10^3) + 73.4V - 0.55V^2 + (1.4 \times 10^{-3})V^3$	A/W
820	$-(3.6 \times 10^3) + 80.5V - 0.61V^2 + (1.5 \times 10^{-3})V^3$	A/W
940	$-(1.9 \times 10^3) + 42.6V - 0.32V^2 + (8 \times 10^{-4})V^3$	A/W
APD8; temperature, 19.9°C; $100 < V < 215$ V		
720	$-(2.1 \times 10^9) + (3.98 \times 10^7)V - (2.5 \times 10^5)V^2 + (5 \times 10^2)V^3$	V/W
820	$-(2.25 \times 10^9) + (4.2 \times 10^7)V - (2.6 \times 10^5)V^2 + (5.35 \times 10^2)V^3$	V/W
940	$-(1.4 \times 10^9) + (2.69 \times 10^7)V - (1.66 \times 10^5)V^2 + (3.4 \times 10^2)V^3$	V/W
APD7; temperature, 22.1°C; $100 < V < 380$ V		
720	$(3.81 \times 10^7) - (9.19 \times 10^6)V + (7.83 \times 10^3)V^2 - 27.1V^3 + (3.33 \times 10^{-2})V^4$	V/W
820	$(5.07 \times 10^7) - (1.22 \times 10^6)V + (1.04 \times 10^4)V^2 - 36.1V^3 + (4.45 \times 10^{-2})V^4$	V/W
940	$(6.28 \times 10^7) - (1.52 \times 10^6)V + (1.29 \times 10^4)V^2 - 44.7V^3 + (5.52 \times 10^{-2})V^4$	V/W
APD6; temperature, 22.6°C; $100 < V < 350$ V		
720	$(4.02 \times 10^8) - (8.77 \times 10^6)V + (6.80 \times 10^4)V^2 - 222.5V^3 + 0.263V^4$	V/W
820	$(4.61 \times 10^8) - (10.02 \times 10^6)V + (7.75 \times 10^4)V^2 - 253.2V^3 + 0.299V^4$	V/W
940	$(2.96 \times 10^8) - (6.35 \times 10^6)V + (4.89 \times 10^4)V^2 - 159.4V^3 + 0.188V^4$	V/W
APD5; temperature, 20.0°C; $2050 < V < 2350$ V		
720	$-(1.73 \times 10^4) + 24.54V - 0.012V^2 + (0.184 \times 10^{-5})V^3$	A/W
820	$-(1.75 \times 10^4) + 24.79V - 0.012V^2 + (0.186 \times 10^{-5})V^3$	A/W
940	$-(0.94 \times 10^4) + 13.25V - 0.006V^2 + (0.099 \times 10^{-5})V^3$	A/W
APD2; temperature, 23.1°C; $310 < V < 340$ V		
720	$-(1.71 \times 10^4) + (1.68 \times 10^2)V - 0.551V^2 + (6.05 \times 10^{-4})V^3$	A/W
820	$-(3.28 \times 10^4) + (3.16 \times 10^2)V - 1.018V^2 + (1.095 \times 10^{-3})V^3$	A/W
940	$-(4.44 \times 10^4) + (4.25 \times 10^2)V - 1.36V^2 + (1.45 \times 10^{-3})V^3$	A/W

Table 3. APD Responsivity Uniformity Scan Measurement Results

APD	Active area, mm^2	Area nonuniformity, percent	Scan array size, μm	Step, μm
APD11	0.2376	14.96	41×41	20
APD10	4.9550	18.76	61×61	50
APD9	0.1800	11.27	31×31	20
APD8	0.1820	16.62	31×31	20
APD7	1.5970	15.50	51×51	40
APD6	0.0148	17.64	31×31	10
APD5	18.88	7.40	41×41	150
APD4	0.5464	6.02	36×36	28
APD2	1.6920	6.10	41×41	47

Table 4. APD Noise Measurement Results

APD	λ, nm	I_n	NEP, $fW/Hz^{1/2}$	D^*, $cm\text{-}Hz^{1/2}W$
APD12	720	2.2×10^{-13} $A/Hz^{1/2}$	1.9	2.87×10^{13}
	820		1.9	3.05×10^{13}
	940		3.9	1.63×10^{13}
APD11	720	2.3×10^{-13} $A/Hz^{1/2}$	1.8	2.77×10^{13}
	820		1.7	2.90×10^{13}
	940		3.1	1.57×10^{13}
APD10	720	2.5×10^{-12} $A/Hz^{1/2}$	74.3	2.99×10^{12}
	820		69.3	3.21×10^{12}
	940		129.4	1.72×10^{12}
APD9	720	1.9×10^{-12} $A/Hz^{1/2}$	80.7	5.26×10^{11}
	820		74.9	5.67×10^{11}
	940		141.8	2.99×10^{11}
APD8	720	9.3×10^{-8} $V/Hz^{1/2}$	11.8	3.62×10^{12}
	820		11.0	3.88×10^{12}
	940		17.7	2.41×10^{12}
APD2	720	1.7×10^{-12} $A/Hz^{1/2}$	28.0	4.75×10^{12}
	820		22.2	5.99×10^{12}
	940		19.4	6.84×10^{12}

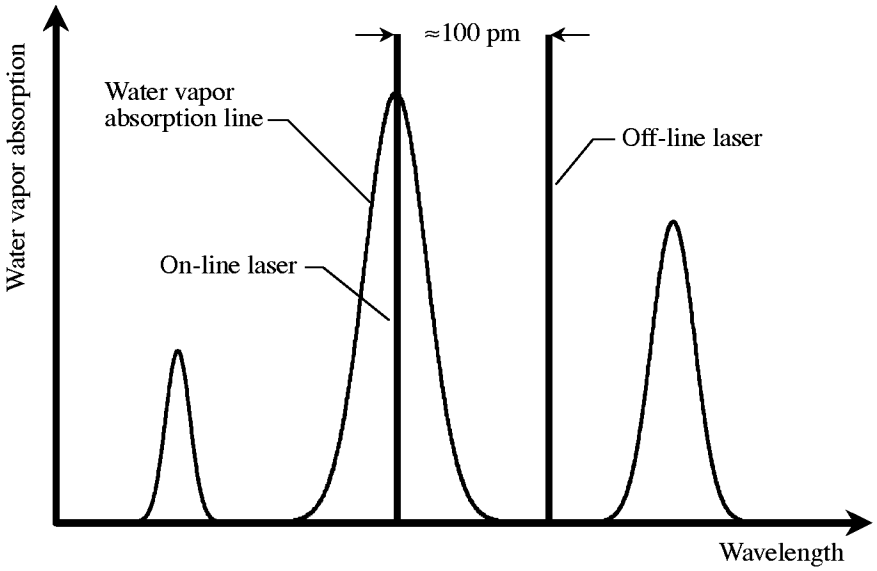

Figure 1. DIAL on-line and off-line wavelengths relative to water vapor absorption line.

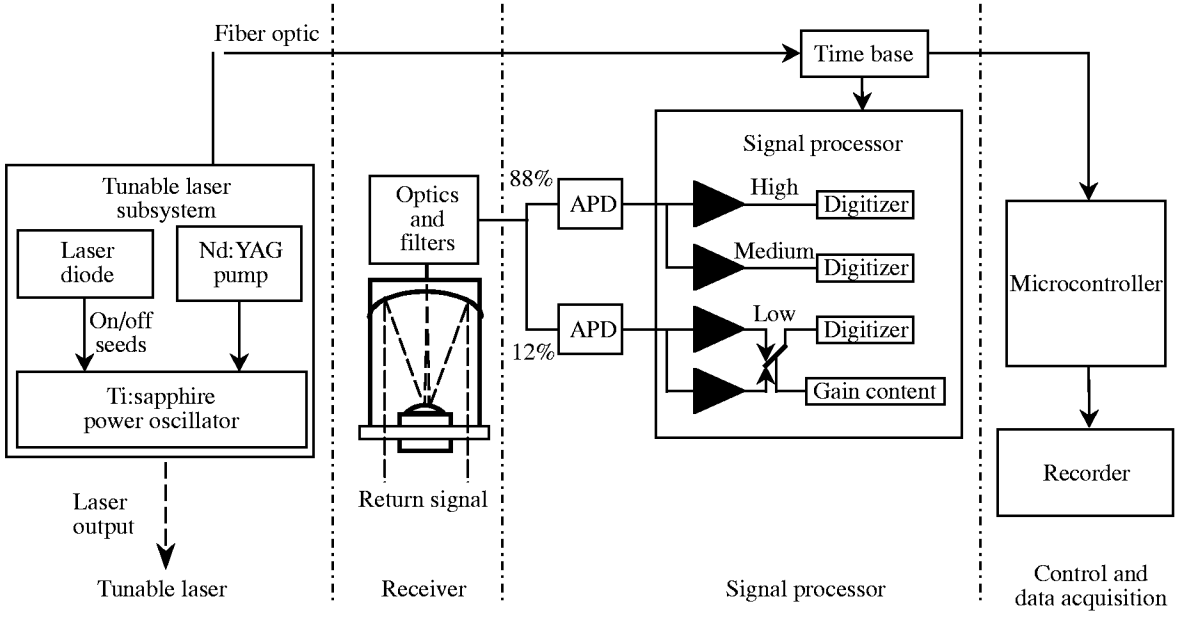

Figure 2. LASE system block diagram.

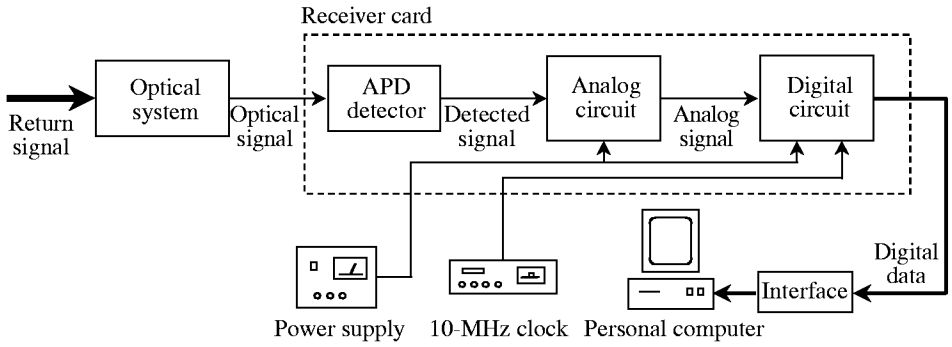

Figure 3. Developed DIAL receiver system.

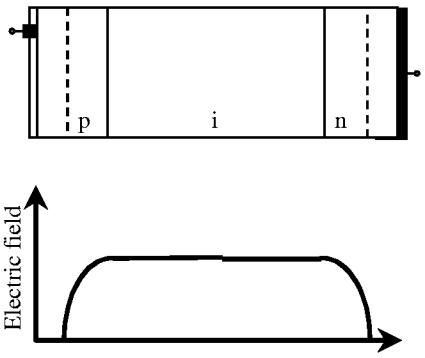

(a) p-i-n diode structure and electric field distribution.

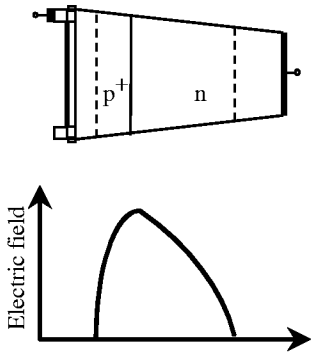

(b) Beveled-edge or deep diffusion APD structure and electric field distribution.

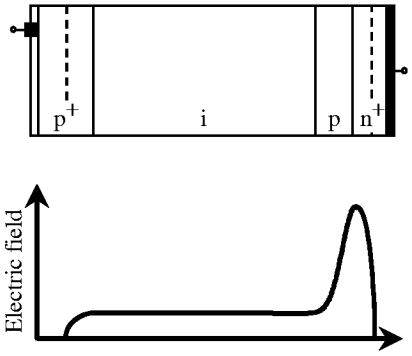

(c) Reach-through APD structure and electric field distribution.

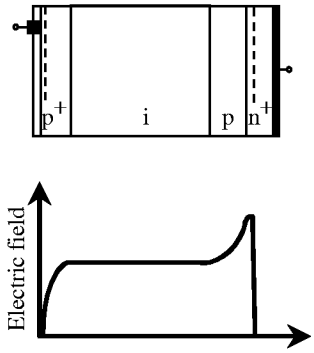

(d) SLIK APD structure and electric field distribution.

Figure 4. p-i-n diode and different APD structures with electric field distributions.

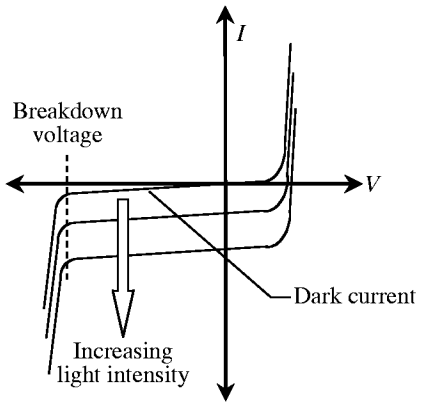

(a) Theoretical, showing breakdown voltage and dark current.

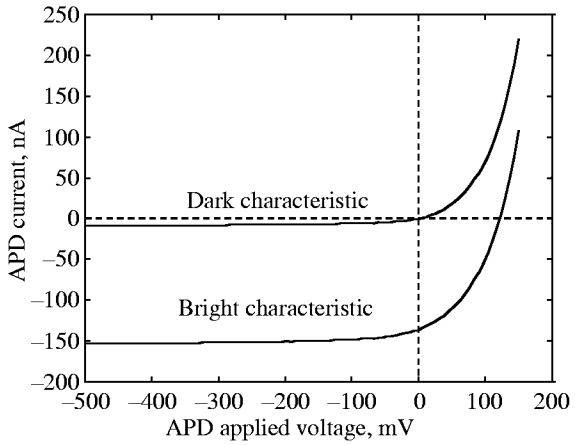

(b) Experimental, measured in dark and bright conditions for APD2.

Figure 5. APD *V-I* characteristics.

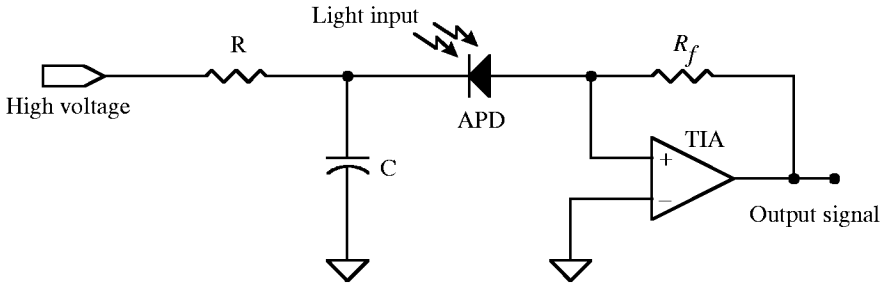

Figure 6. APD package circuit.

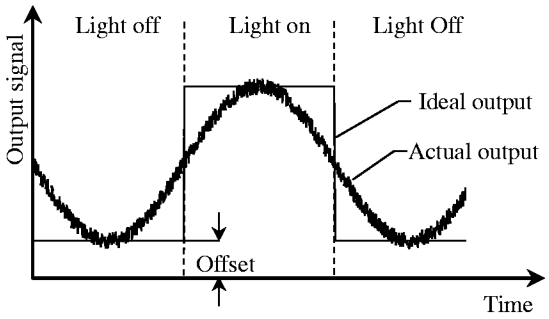

(a) Ideal and actual signals.

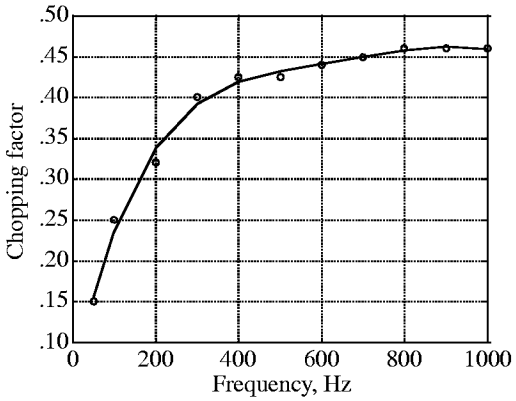

(b) Chopping factor versus chopping frequency.

Figure 7. Output of chopper experiment.

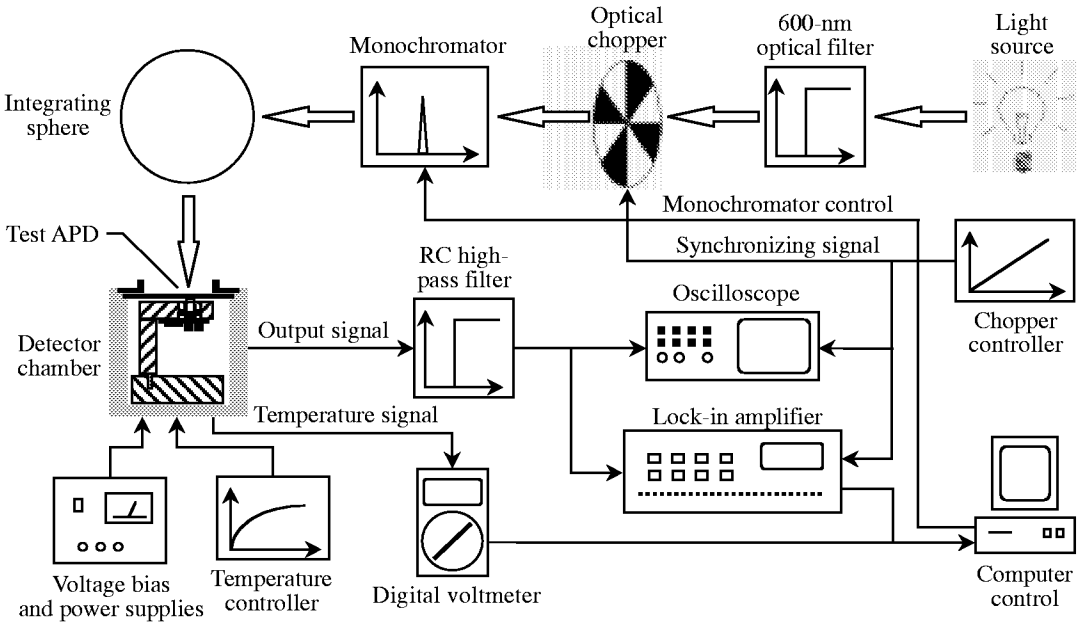

Figure 8. Optical and electrical setup to determine APD spectral response.

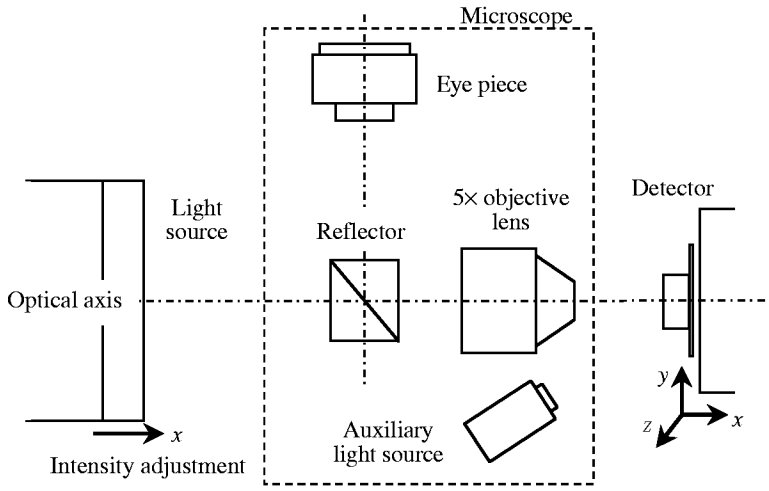

Figure 9. APD alignment using microscope.

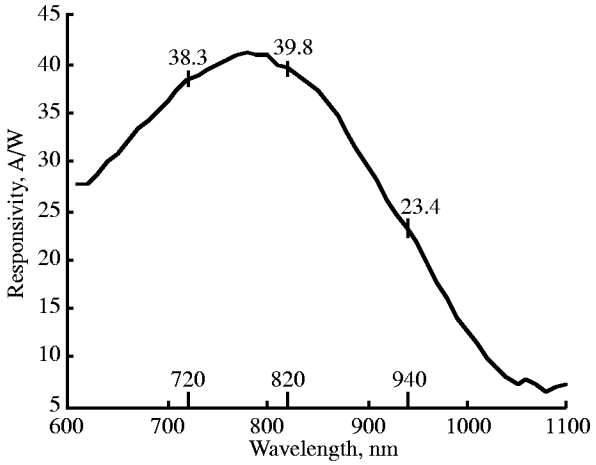

(a) APD12 at 336 V and 25°C.

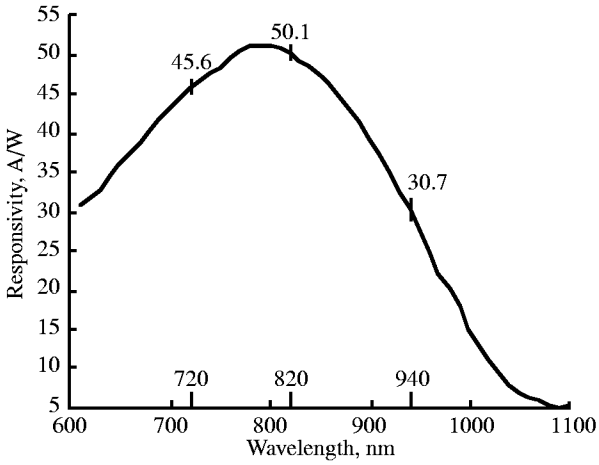

(b) APD11 at 415 V and 23°C.

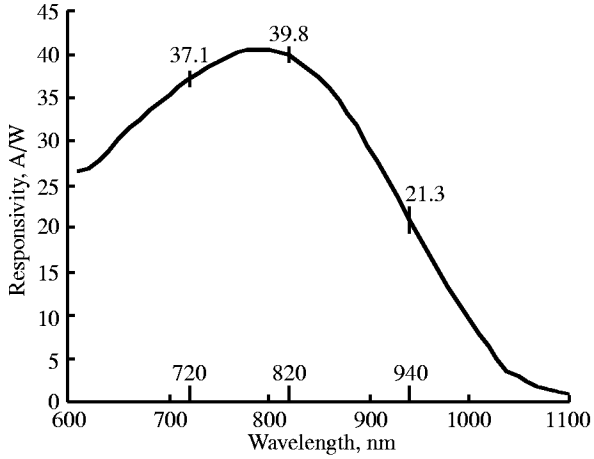

(c) APD10 at 110 V and 22.3°C.

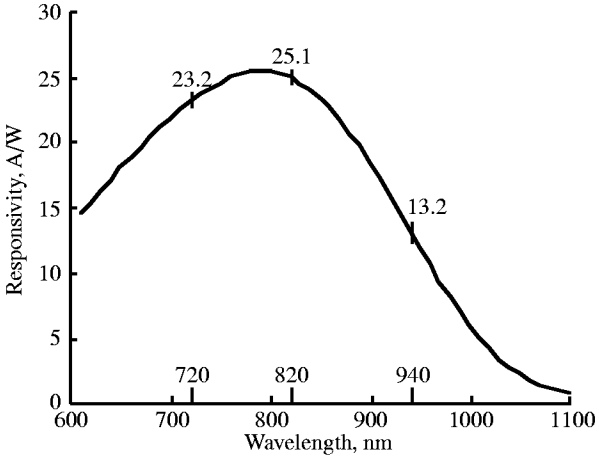

(d) APD9 at 150 V and 21.9°C.

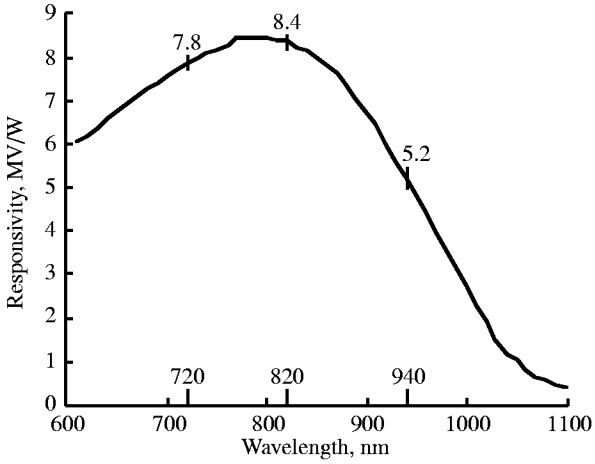

(e) APD8 at 190 V and 23°C.

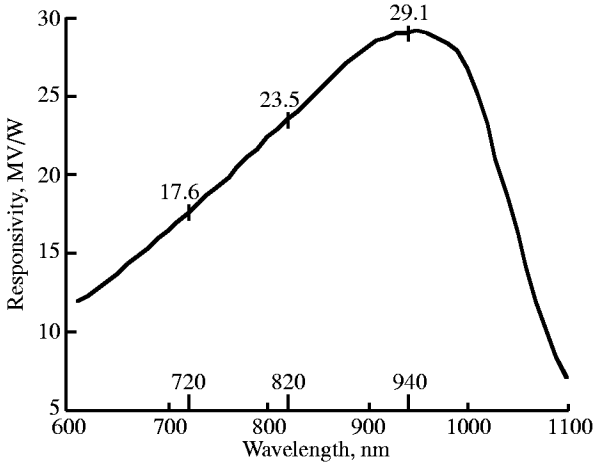

(f) APD7 at 380 V and 23.6°C.

Figure 10. APD spectral response calibration.

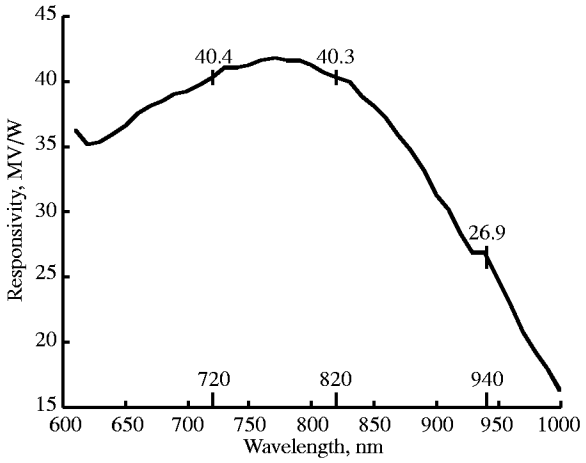

(g) APD6 at 410 V and 22.2°C.

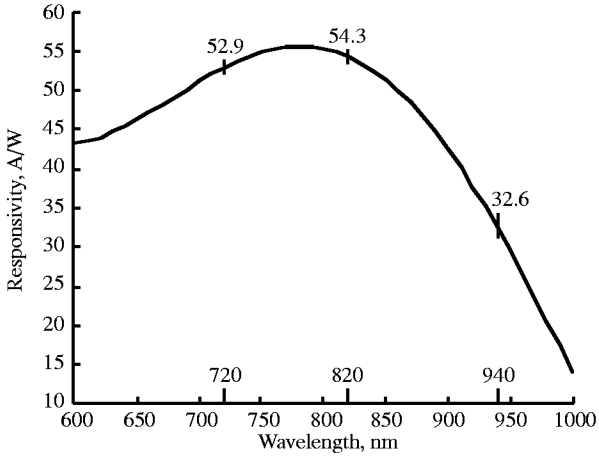

(h) APD5 at 317 V and 2350 V.

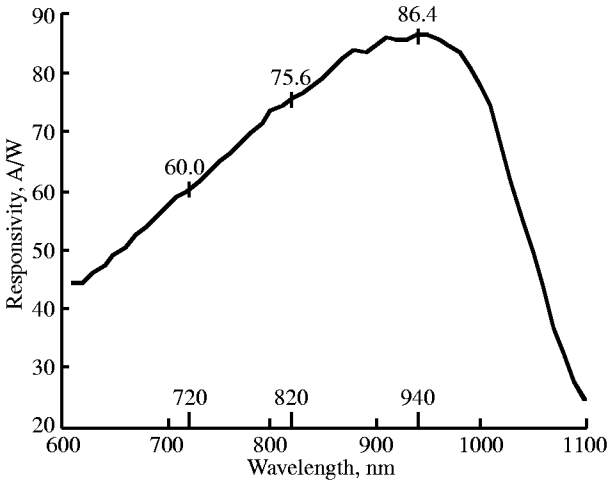

(i) APD2 at 317 V and 23.1°C.

Figure 10. Concluded.

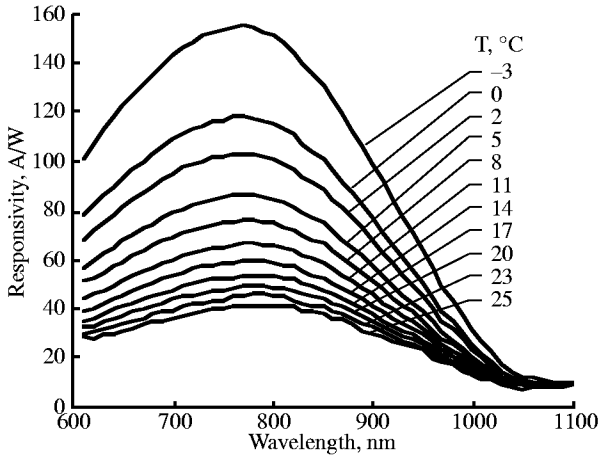

(a) APD12 at 336-V bias voltage for various temperatures.

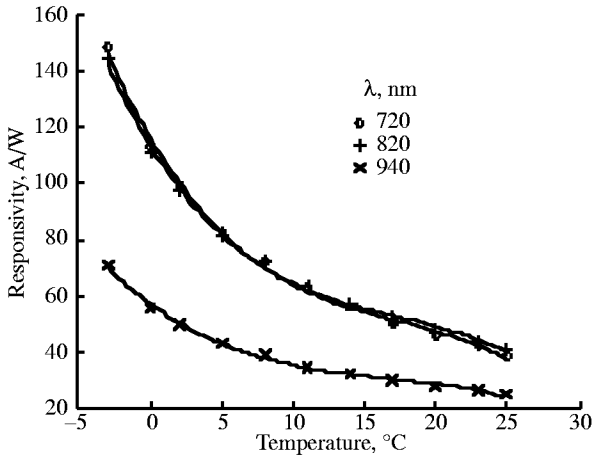

(b) APD12 at 336-V bias voltage for various wavelengths.

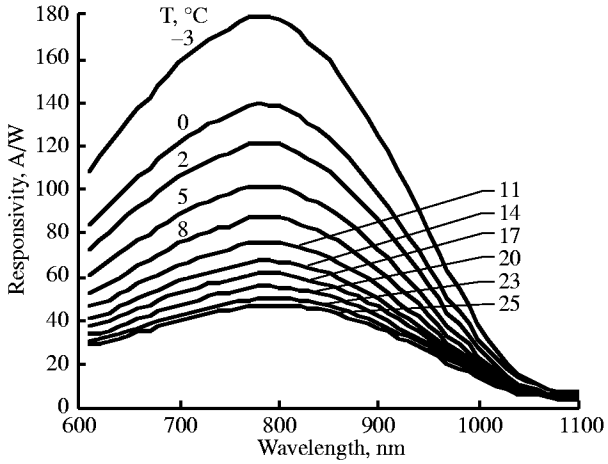

(c) APD11 at 415-V bias voltage for various temperatures.

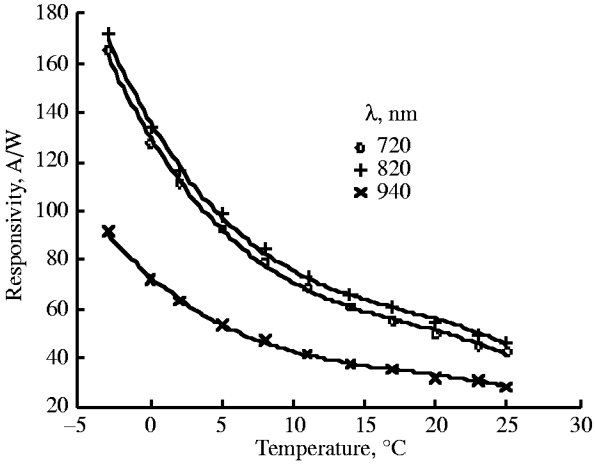

(d) APD11 at 415-V bias voltage for various wavelengths.

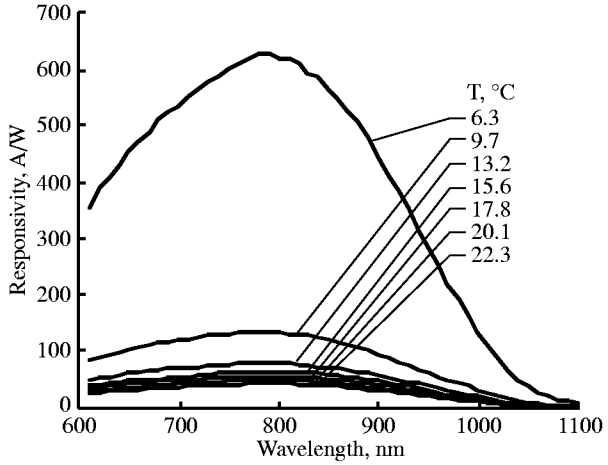

(e) APD10 at 110-V bias voltage for various temperatures.

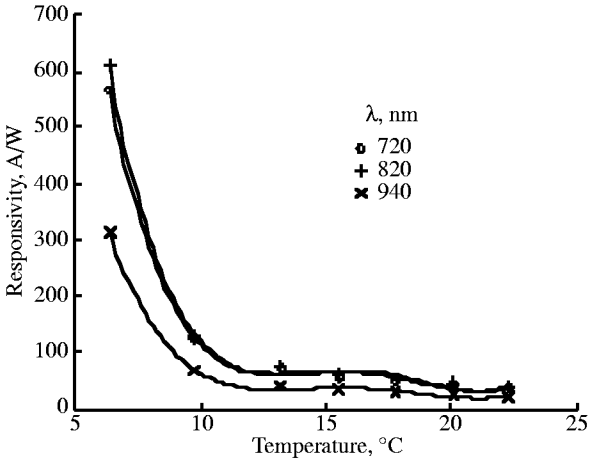

(f) APD10 at 110-V bias voltage for various wavelengths.

Figure 11. Responsivity variation of wavelength λ and temperature *T*.

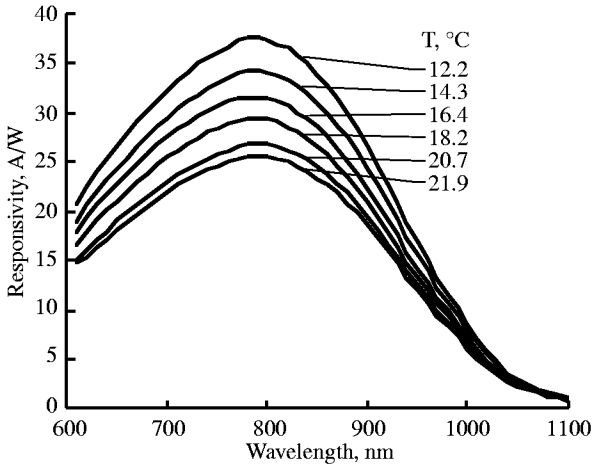

(g) APD9 at 150-V bias voltage for various temperatures.

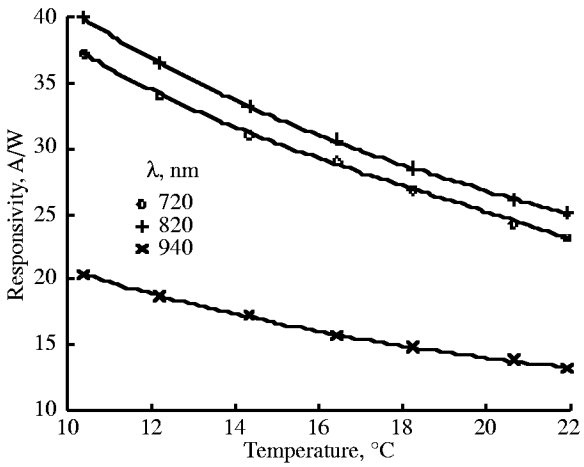

(h) APD9 at 150-V bias voltage for various wavelengths.

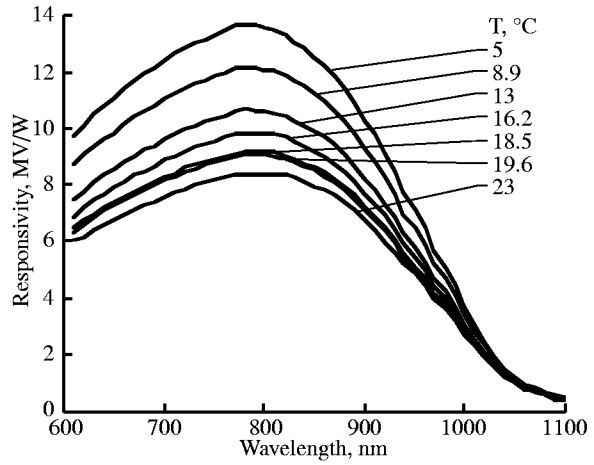

(i) APD8 at 190-V bias voltage for various temperatures.

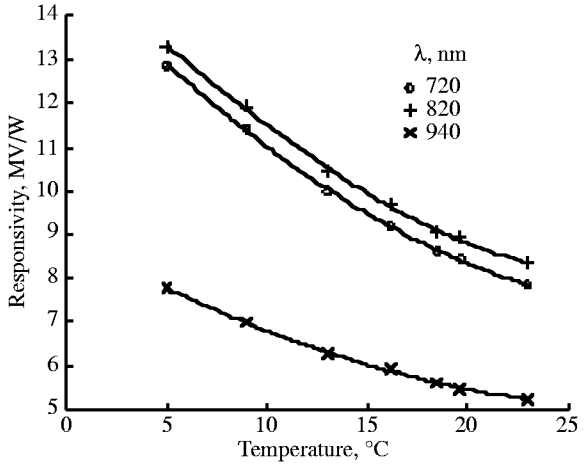

(j) APD8 at 190-V bias voltage for various wavelengths.

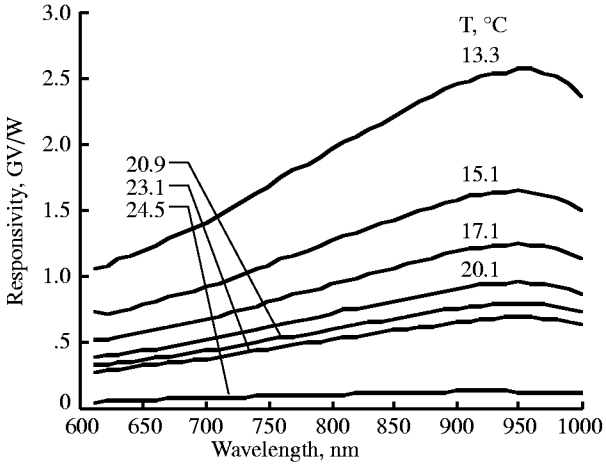

(k) APD7 at 380-V bias voltage for various temperatures.

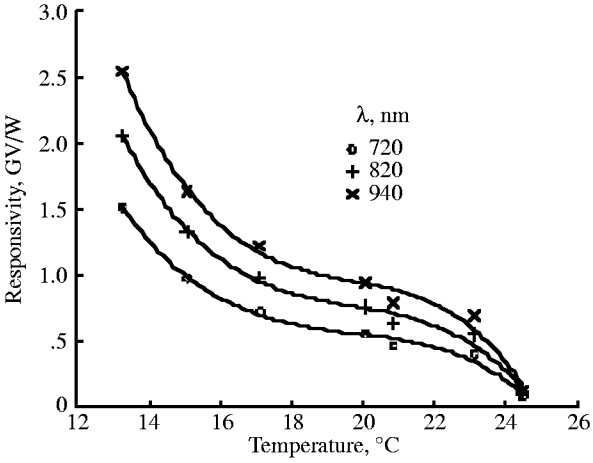

(l) APD7 at 380-V bias voltage for various wavelengths.

Figure 11. Continued.

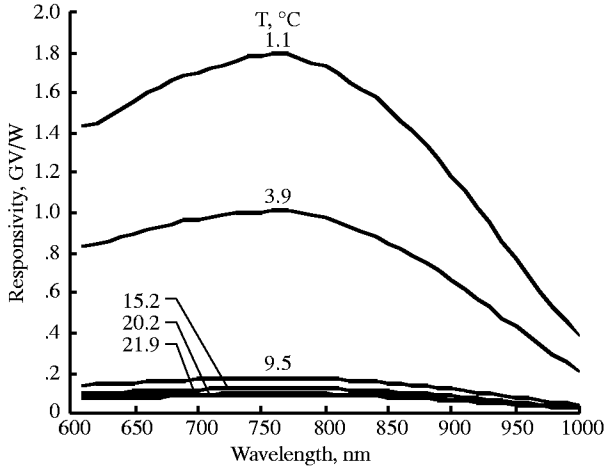

(m) APD6 at 410-V bias voltage for various temperatures.

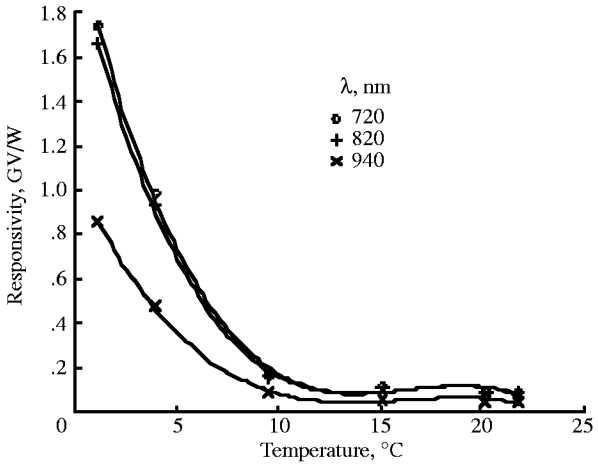

(n) APD6 at 410-V bias voltage for various wavelengths.

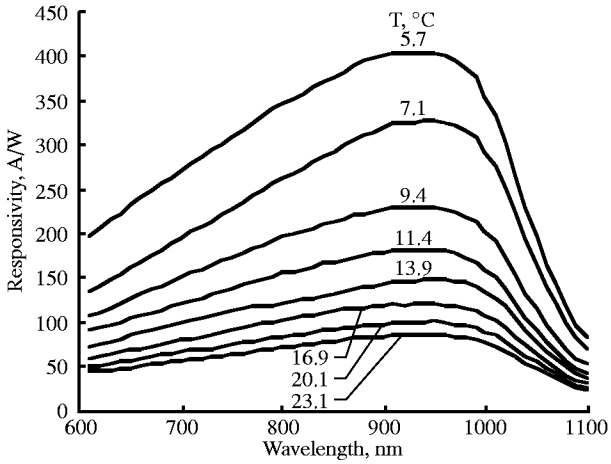

(o) APD2 at 317-V bias voltage for various temperatures.

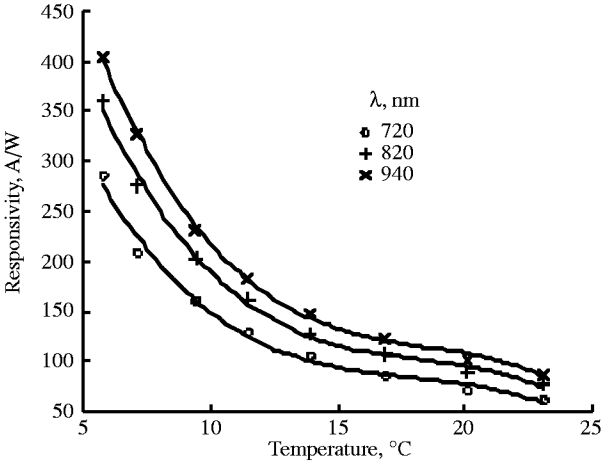

(p) APD2 at 317-V bias voltage for various wavelengths.

Figure 11. Concluded.

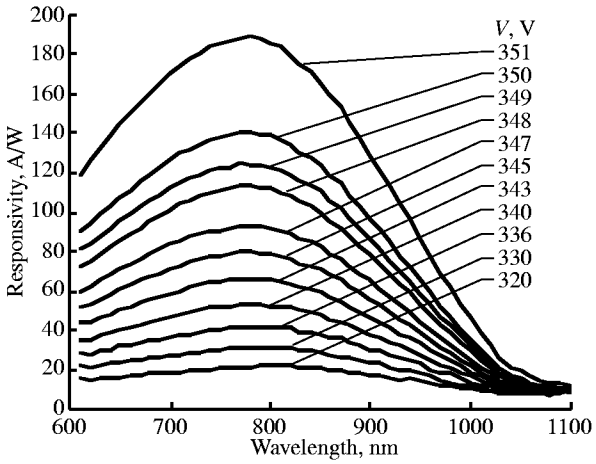

(a) APD12 at 25°C for various bias voltages.

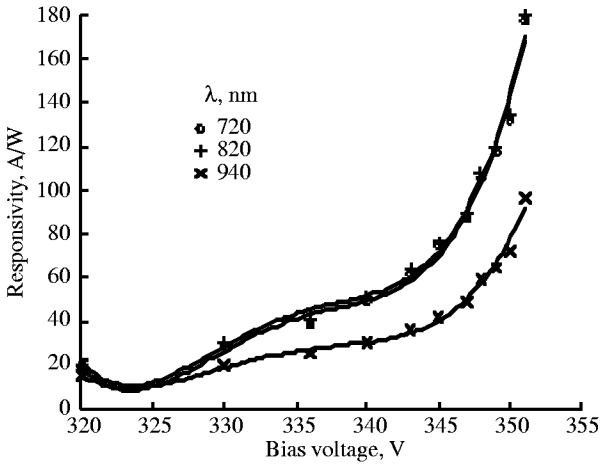

(b) APD12 at 25°C for various wavelengths.

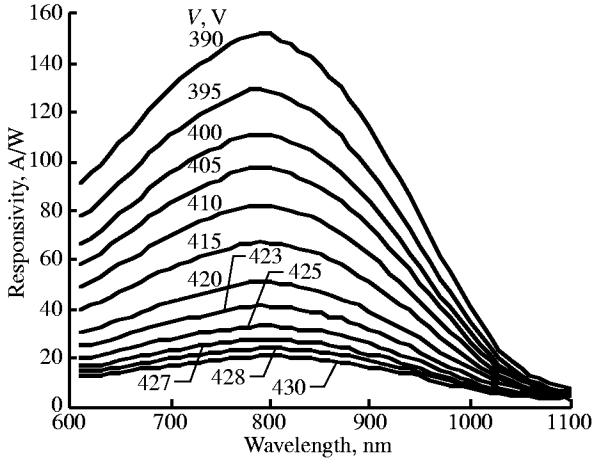

(c) APD11 at 23°C for various bias voltages.

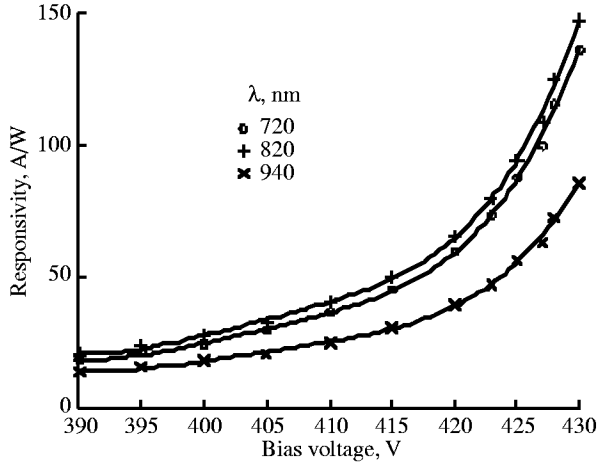

(d) APD11 at 23°C for various wavelengths.

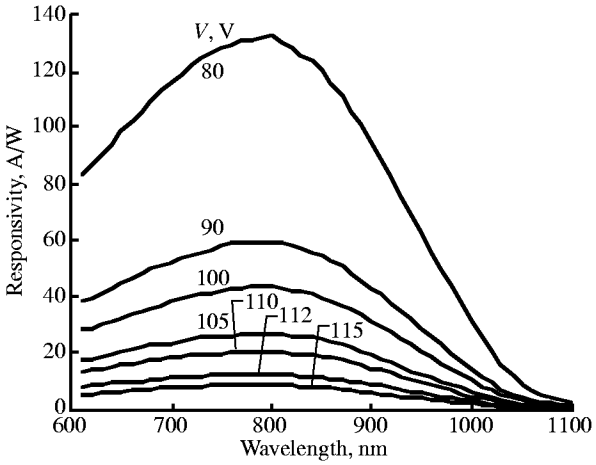

(e) APD10 at 20.9°C for various bias voltages.

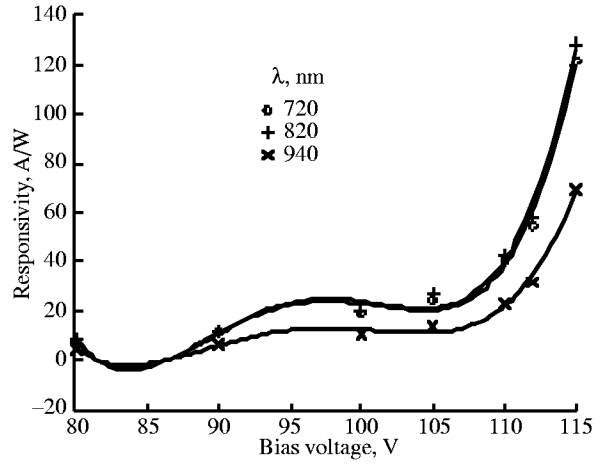

(f) APD10 at 20.9°C for various wavelengths.

Figure 12. Responsivity variation of wavelength λ and voltage V.

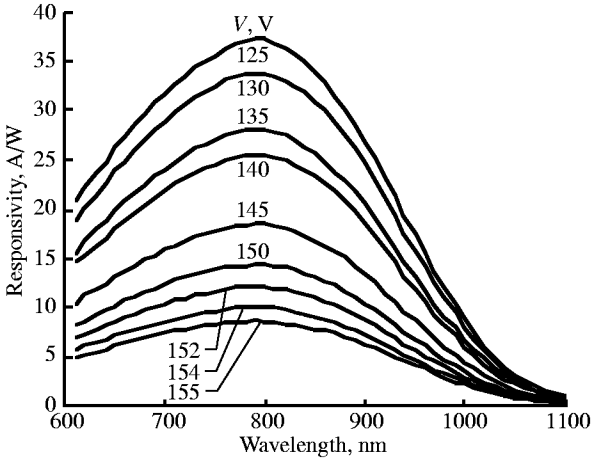

(g) APD9 at 22°C for various bias voltages.

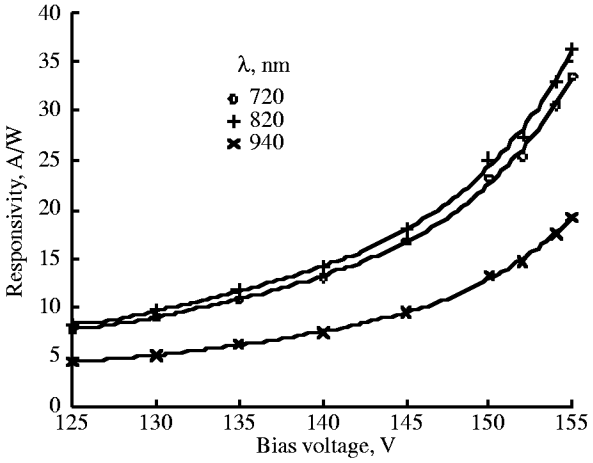

(h) APD9 at 25°C for various wavelengths.

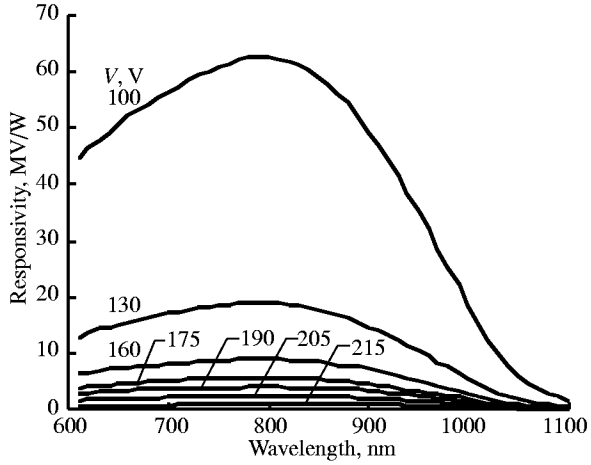

(i) APD8 at 19.9°C for various bias voltages.

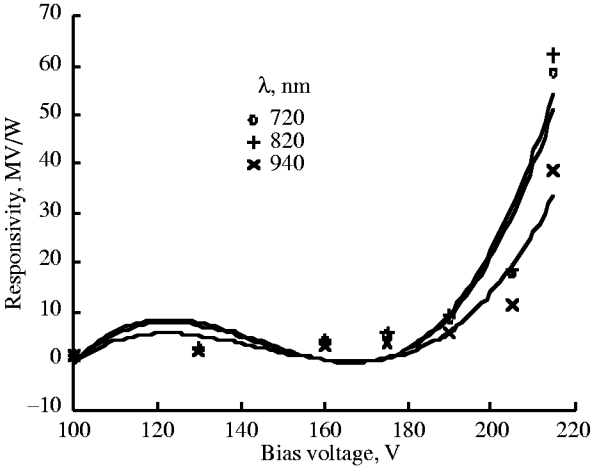

(j) APD8 at 19.9°C for various wavelengths.

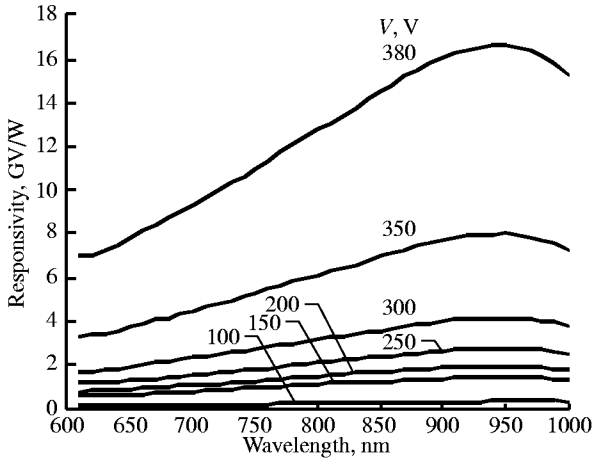

(k) APD7 at 22.1°C for various bias voltages.

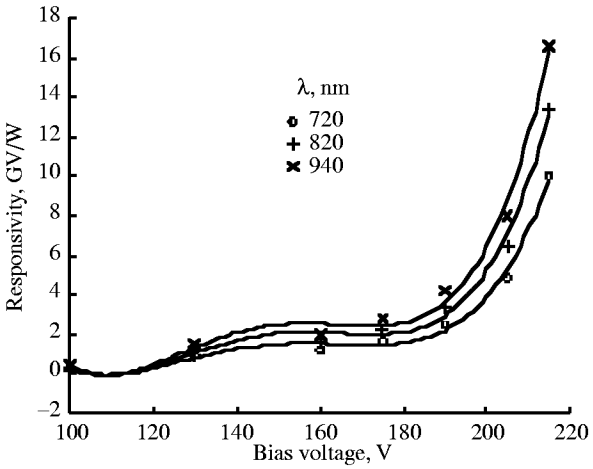

(l) APD7 at 22.1°C for various wavelengths.

Figure 12. Continued.

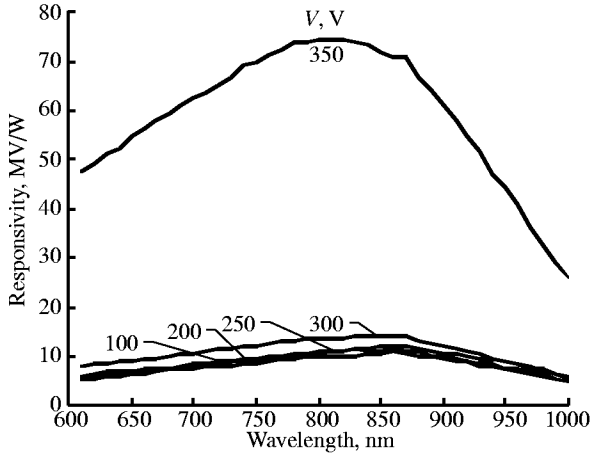

(m) APD6 at 22.6°C for various bias voltages.

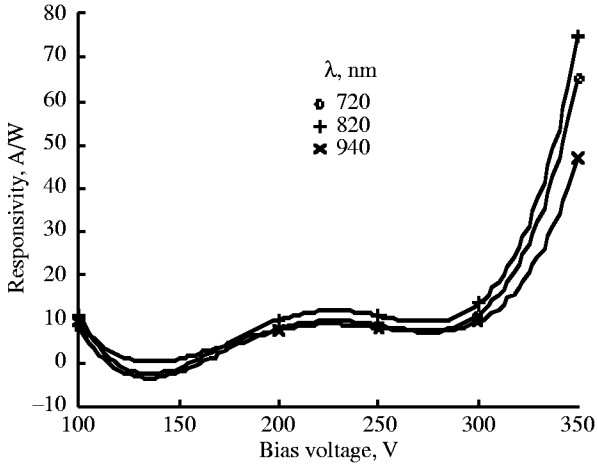

(n) APD6 at 22.6°C for various wavelengths.

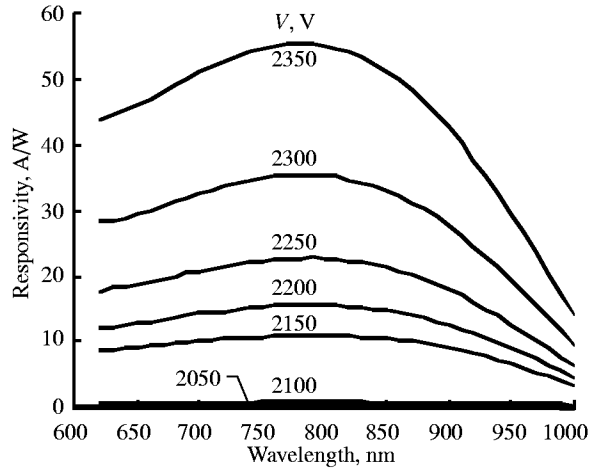

(o) APD5 at 20°C for various bias voltages.

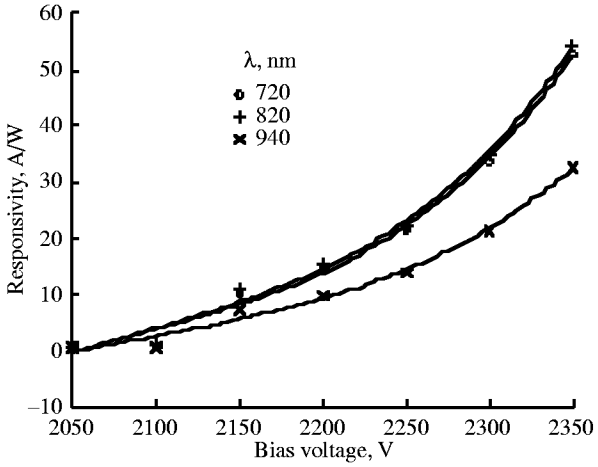

(p) APD5 at 20°C for various wavelengths.

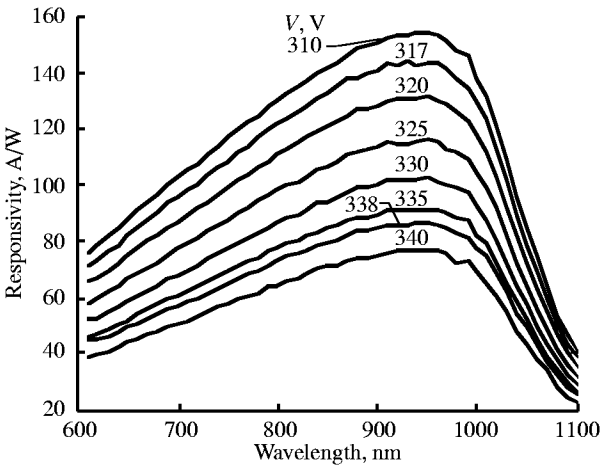

(q) APD2 at 23.1°C for various bias voltages.

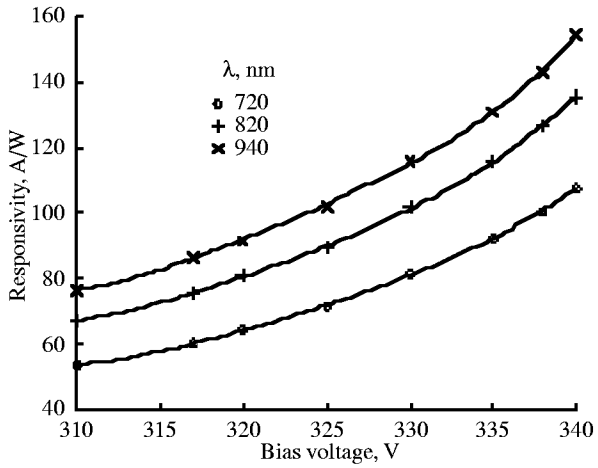

(r) APD2 at 23.1°C for various wavelengths.

Figure 12. Concluded.

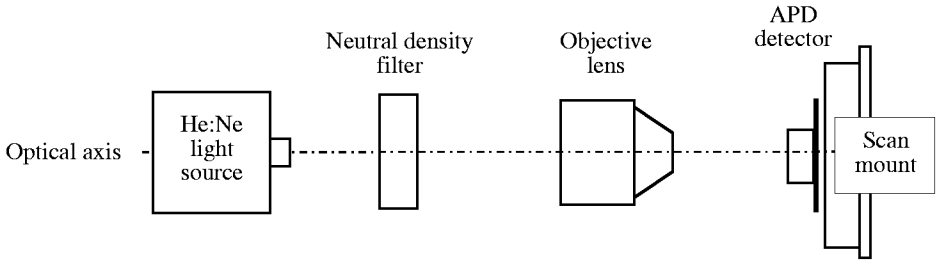

Figure 13. Responsivity uniformity scan setup.

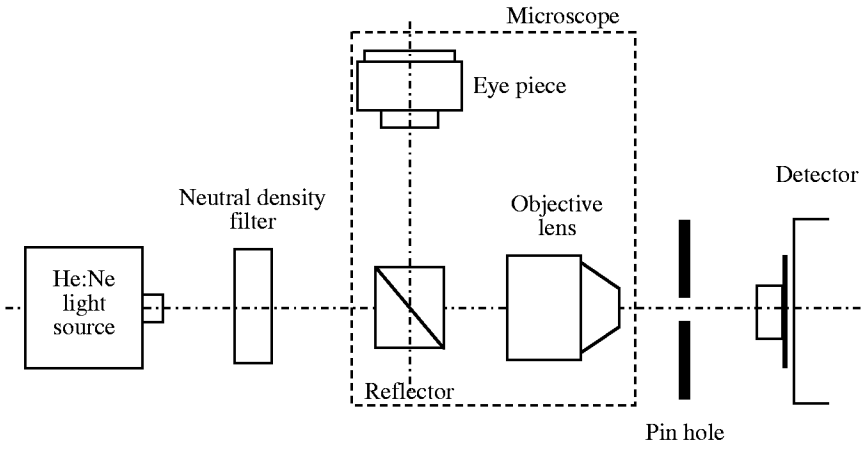

Figure 14. Laser focal point evaluation setup.

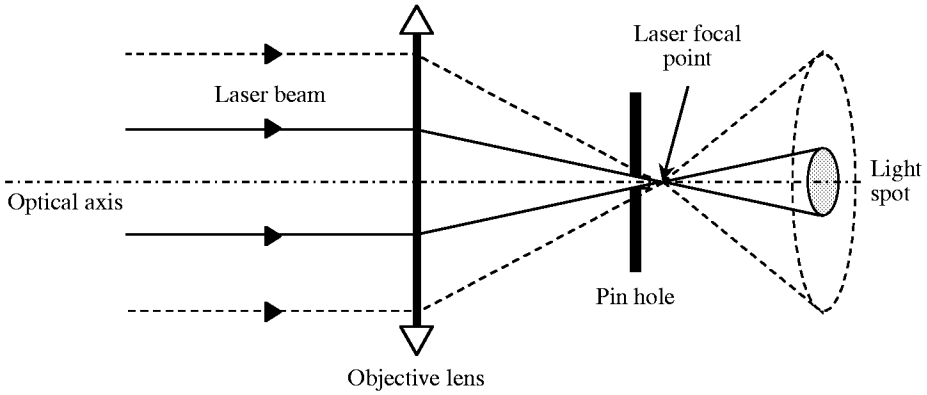

Figure 15. Laser focal point evaluation using pin hole.

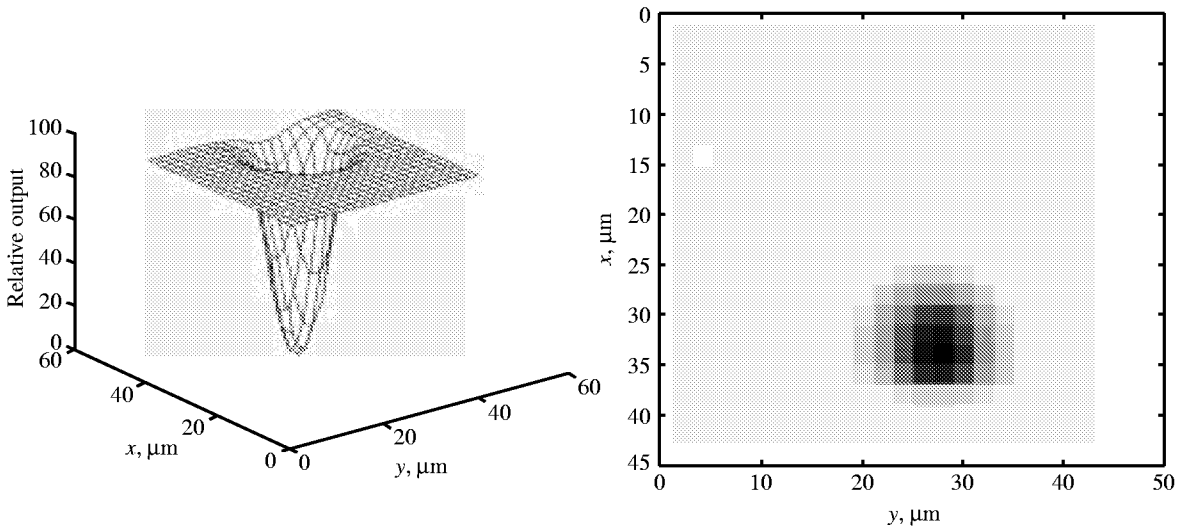

Figure 16. Pin hole uniformity scan.

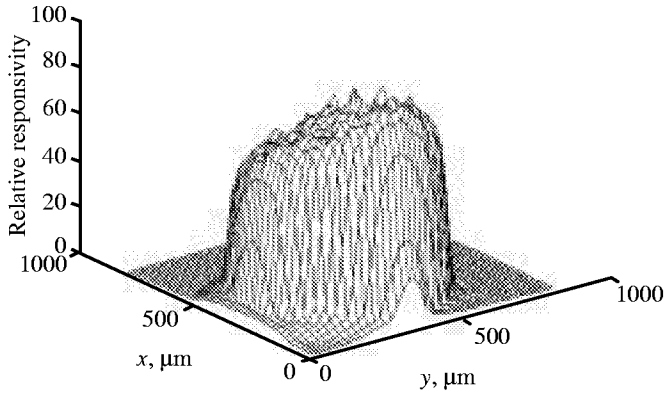

(a) APD11 responsivity uniformity scan.

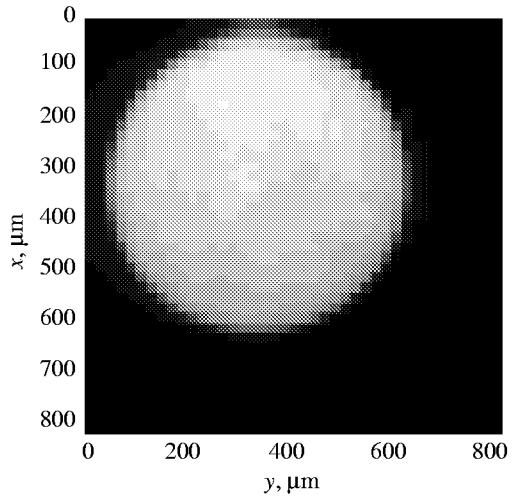

(b) APD11 active area.

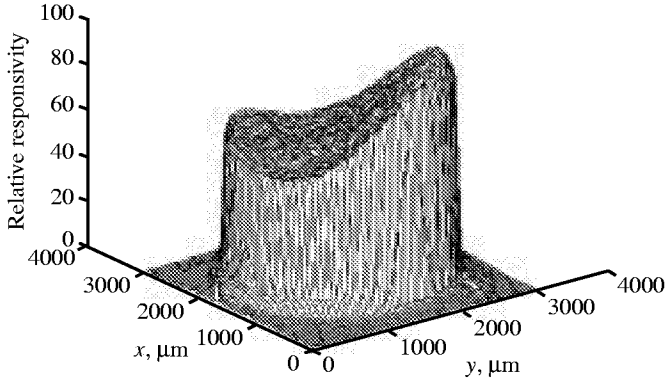

(c) APD10 responsivity uniformity scan.

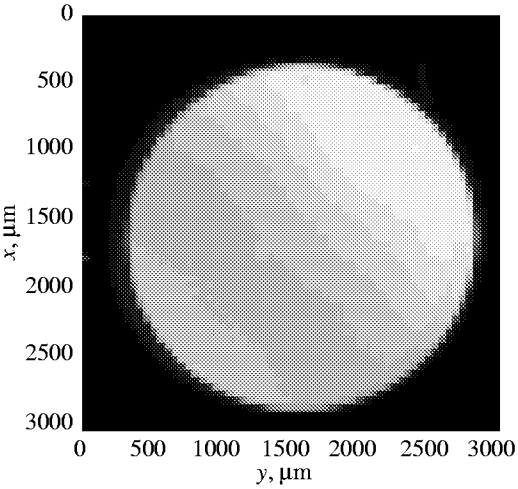

(d) APD10 active area.

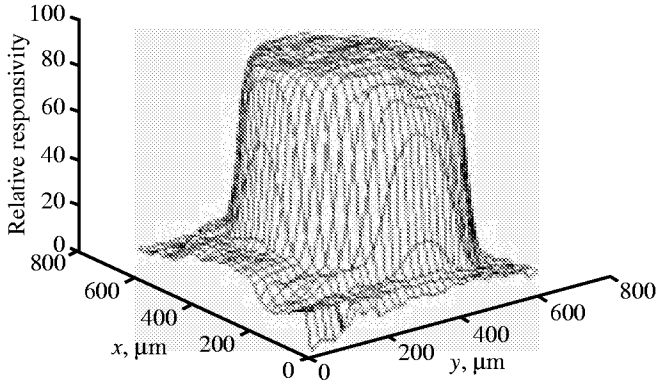

(e) APD9 responsivity uniformity scan.

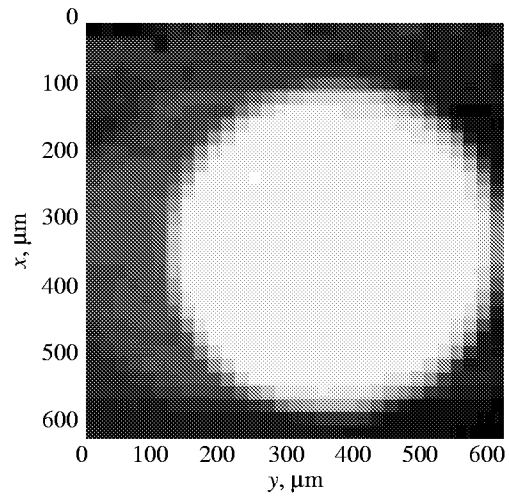

(f) APD9 active area.

Figure 17. APD active area scan results.

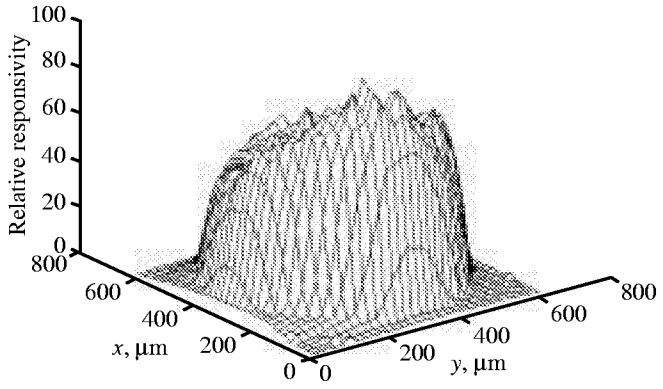

(g) APD8 responsivity uniformity scan.

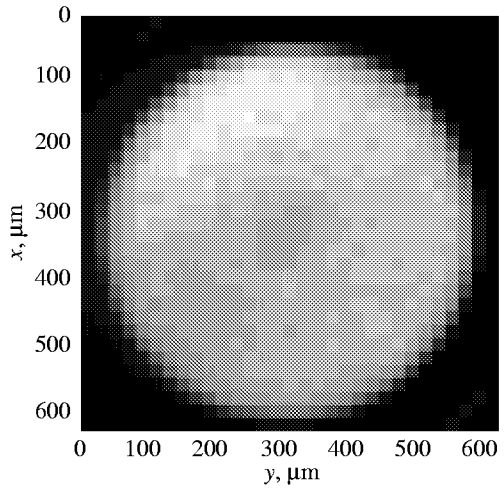

(h) APD8 active area.

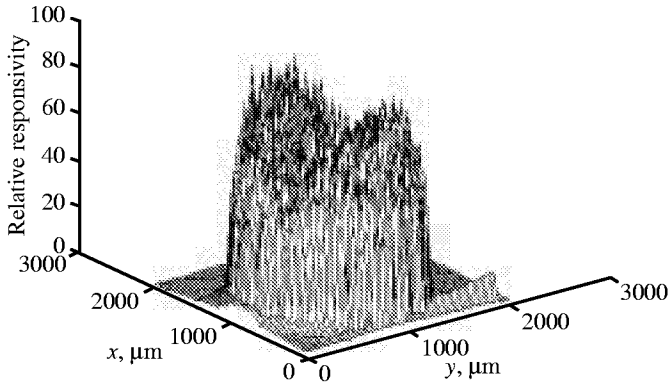

(i) APD7 responsivity uniformity scan.

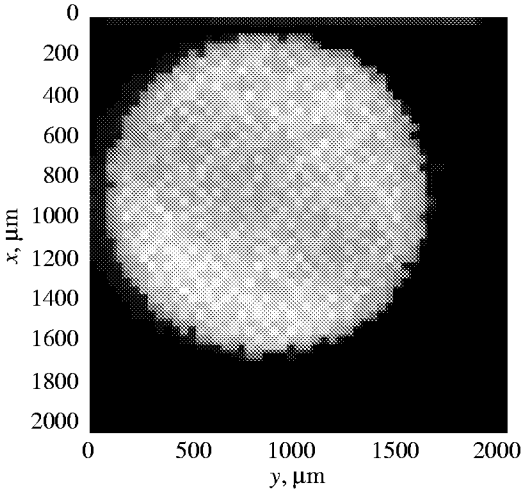

(j) APD7 active area.

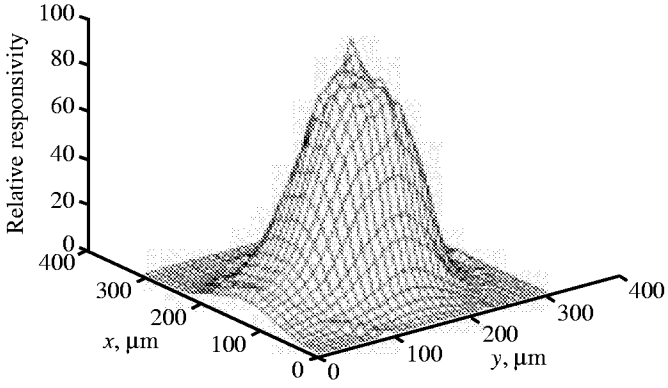

(k) APD6 responsivity uniformity scan.

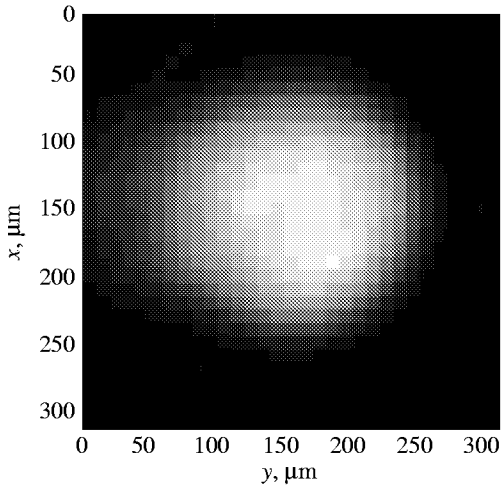

(l) APD6 active area.

Figure 17. Continued.

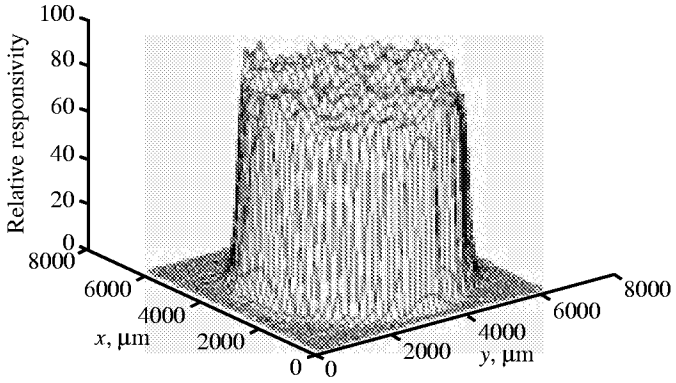

(m) APD5 responsivity uniformity scan.

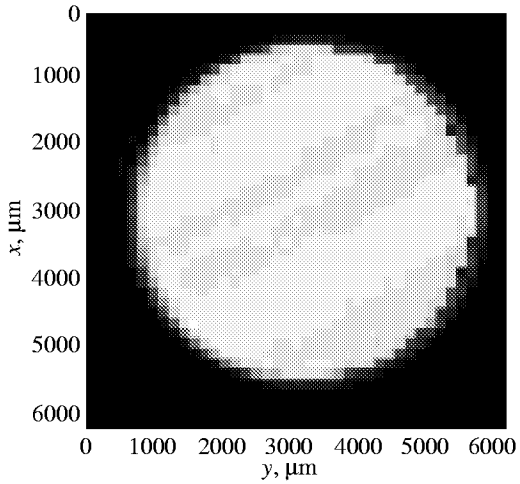

(n) APD5 active area.

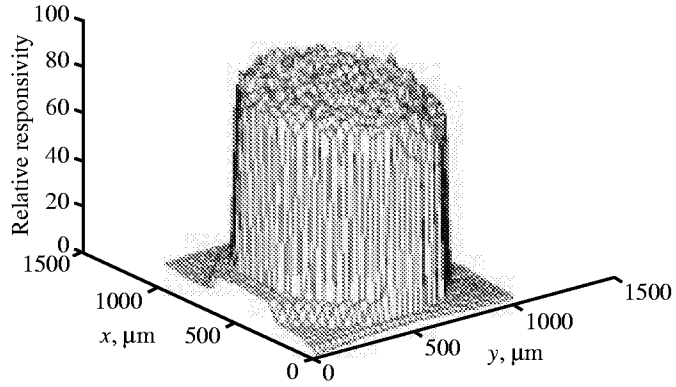

(o) APD4 responsivity uniformity scan.

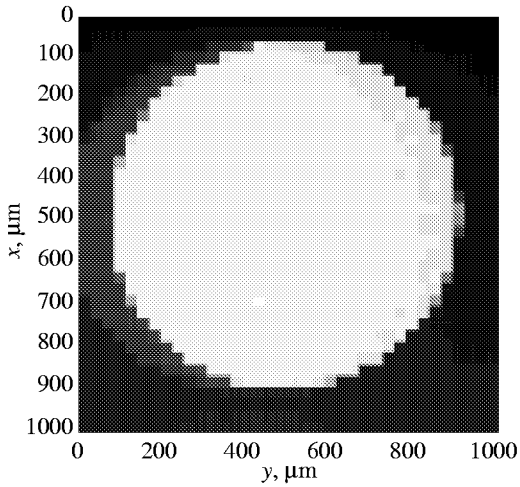

(p) APD4 active area.

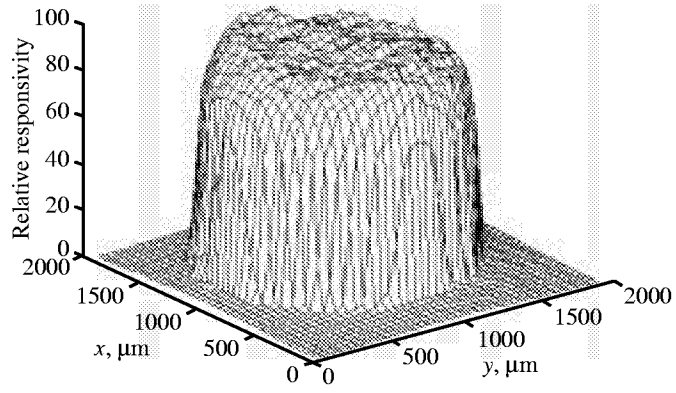

(q) APD2 responsivity uniformity scan.

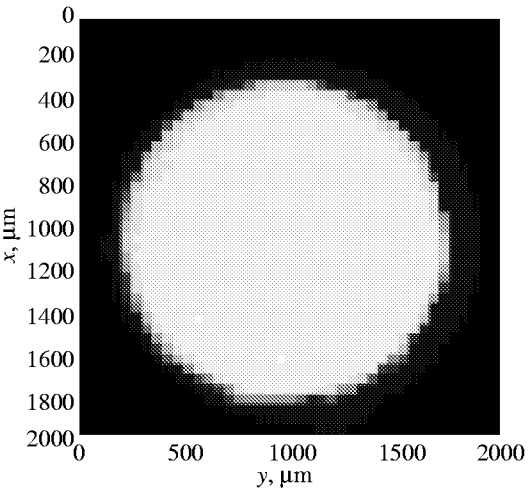

(r) APD2 active area.

Figure 17. Concluded.

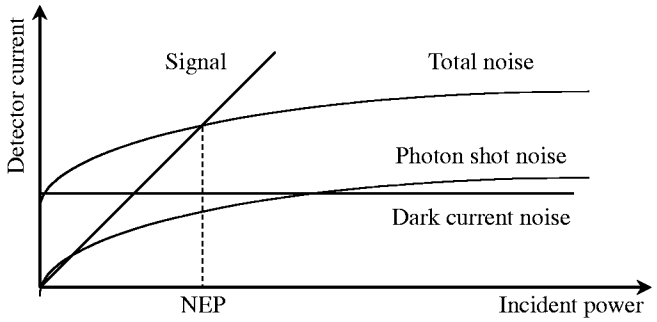

Figure 18. Noise as function of optical power incident on detector.

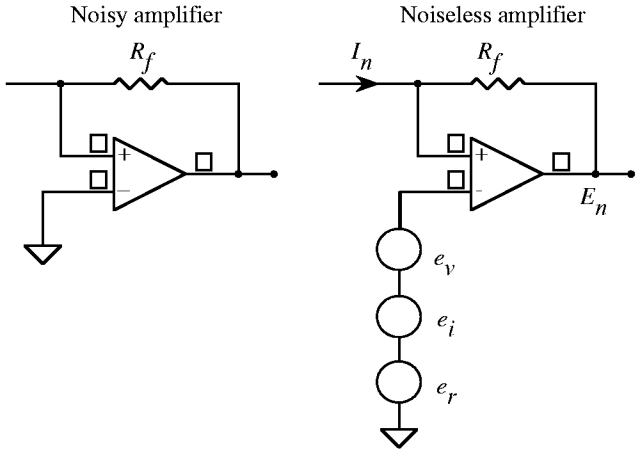

Figure 19. Separation of TIA noise sources.

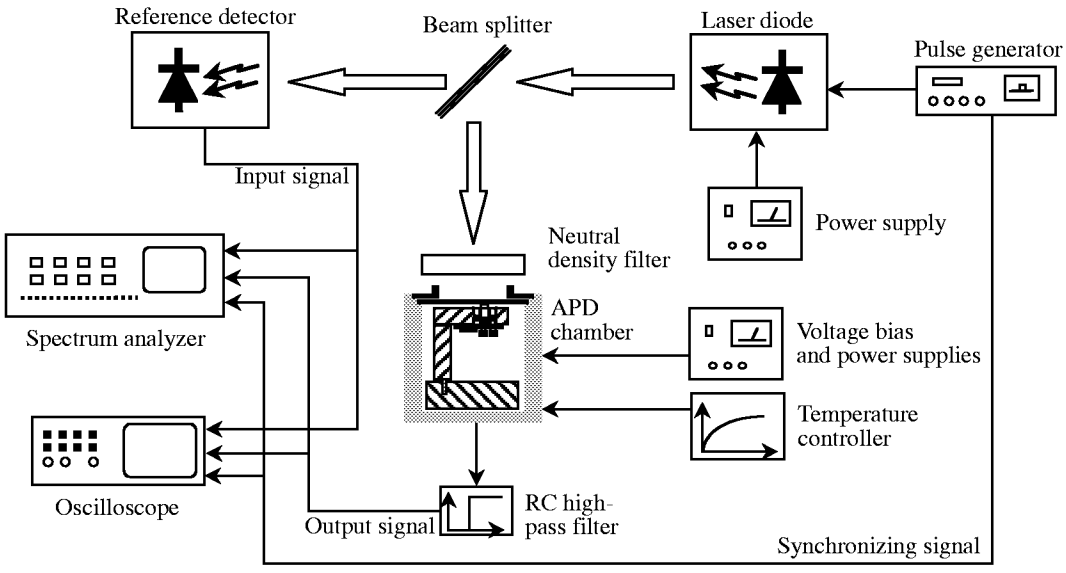

Figure 20. Frequency response experimental setup.

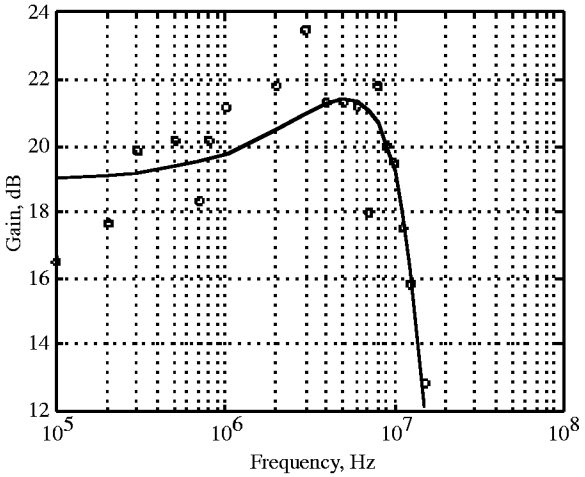

(a) Frequency response.

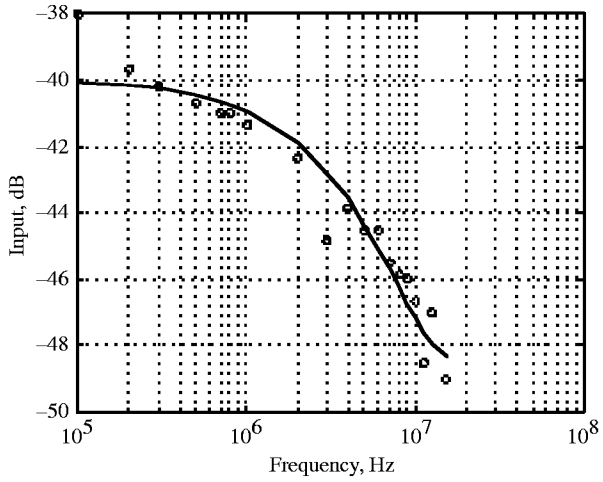

(b) Input.

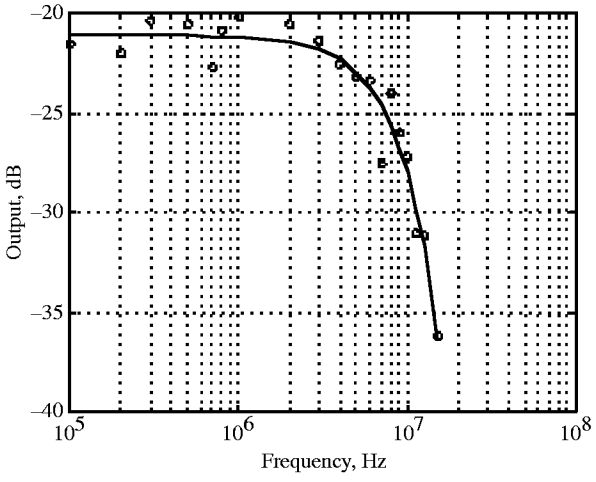

(c) Output.

Figure 21. APD12 frequency spectrum at bias voltage of 336 V and temperature of 23°C. Spectrum in (a) was derived from input in (b) and output in (c).

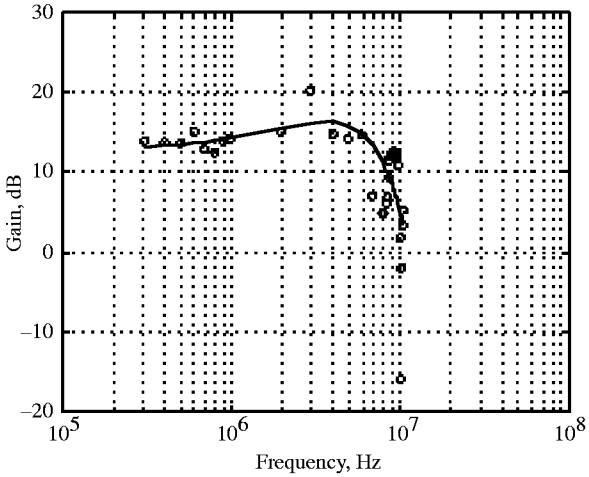

(a) Frequency response.

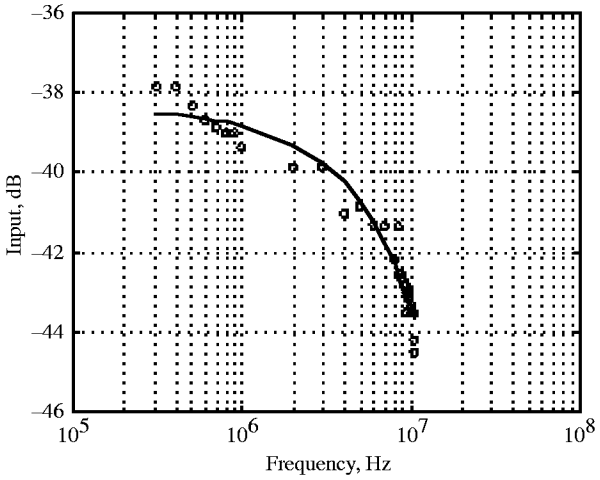

(b) Input.

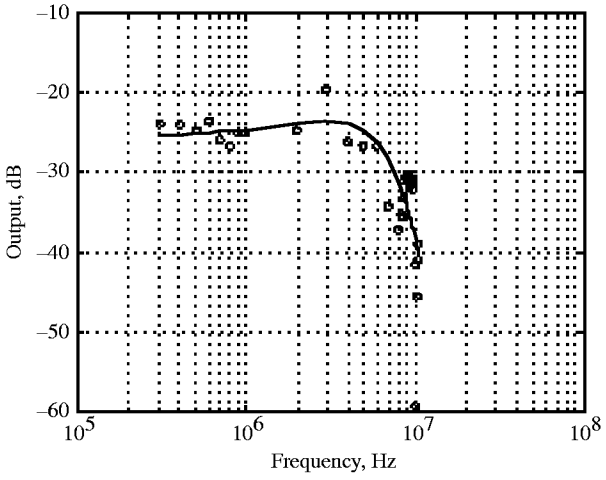

(c) Output.

Figure 22. APD11 frequency spectrum at bias voltage of 415 V and temperature of 23°C. Spectrum in (a) was derived from input in (b) and output in (c).

REPORT DOCUMENTATION PAGE

Form Approved
OMB No. 0704-0188

1. AGENCY USE ONLY *(Leave blank)*	2. REPORT DATE	3. REPORT TYPE AND DATES COVERED
	July 2000	Technical Publication

4. TITLE AND SUBTITLE
Characterization of Advanced Avalanche Photodiodes for Water Vapor Lidar Receivers

5. FUNDING NUMBERS
WU 622-63-13-70

6. AUTHOR(S)
Tamer F. Refaat, Gary E. Halama, and Russell J. DeYoung

7. PERFORMING ORGANIZATION NAME(S) AND ADDRESS(ES)
NASA Langley Research Center
Hampton, VA 23681-2199

8. PERFORMING ORGANIZATION REPORT NUMBER
L-17936

9. SPONSORING/MONITORING AGENCY NAME(S) AND ADDRESS(ES)
National Aeronautics and Space Administration
Washington, DC 20546-0001

10. SPONSORING/MONITORING AGENCY REPORT NUMBER
NASA/TP-2000-210096

11. SUPPLEMENTARY NOTES
Refaat: Old Dominion University, Norfolk, VA; Halama and DeYoung: Langley Research Center, Hampton, VA.

12a. DISTRIBUTION/AVAILABILITY STATEMENT
Unclassified–Unlimited
Subject Category 33 Distribution: Standard
Availability: NASA CASI (301) 621-0390

12b. DISTRIBUTION CODE

13. ABSTRACT *(Maximum 200 words)*

Development of advanced differential absorption lidar (DIAL) receivers is very important to increase the accuracy of atmospheric water vapor measurements. A major component of such receivers is the optical detector. In the near-infrared wavelength range avalanche photodiodes (APD's) are the best choice for higher signal-to-noise ratio, where there are many water vapor absorption lines. In this study, characterization experiments were performed to evaluate a group of silicon-based APD's. The APD's have different structures representative of different manufacturers. The experiments include setups to calibrate these devices, as well as characterization of the effects of voltage bias and temperature on the responsivity, surface scans, noise measurements, and frequency response measurements. For each experiment, the setup, procedure, data analysis, and results are given and discussed. This research was done to choose a suitable APD detector for the development of an advanced atmospheric water vapor differential absorption lidar detection system operating either at 720, 820, or 940 nm. The results point out the benefits of using the super low ionization ratio (SLIK) structure APD for its lower noise-equivalent power, which was found to be on the order of 2 to 4 $fW/Hz^{1/2}$, with an appropriate optical system and electronics. The water vapor detection systems signal-to-noise ratio will increase by a factor of 10.

14. SUBJECT TERMS	15. NUMBER OF PAGES
APD; Reach-through structure; SLIK structure; Beveled-edge structure	62
	16. PRICE CODE: A04

17. SECURITY CLASSIFICATION OF REPORT	18. SECURITY CLASSIFICATION OF THIS PAGE	19. SECURITY CLASSIFICATION OF ABSTRACT	20. LIMITATION OF ABSTRACT
Unclassified	Unclassified	Unclassified	UL